Draft version October 27, 2018
Preprint typeset using LaTeX style emulateapj v. 5/2/11

TYPE IIb SUPERNOVA SN 2011dh: SPECTRA AND PHOTOMETRY FROM THE ULTRAVIOLET TO THE NEAR-INFRARED

G. H. "Howie" Marion[1], Jozsef Vinko[2,3], Robert P. Kirshner[1], Ryan J. Foley[1,4], Perry Berlind[1], Allyson Bieryla[1], Joshua S. Bloom[5], Michael L. Calkins[1], Peter Challis[1], Roger A. Chevalier[6], Ryan Chornock[1], Chris Culliton[7], Jason L. Curtis[7], Gilbert A. Esquerdo[1], Mark E. Everett[8], Emilio E. Falco[1], Kevin France[9], Claes Fransson[10], Andrew S. Friedman[1], Peter Garnavich[11], Bruno Leibundgut[12], Samuel Meyer[1], Nathan Smith[13], Alicia M. Soderberg[1], Jesper Sollerman[10], Dan L. Starr[5], Tamas Szklenar[1], Katalin Takats[3,14] and J. Craig Wheeler[2]

Draft version October 27, 2018

ABSTRACT

We report spectroscopic and photometric observations of the Type IIb SN 2011dh obtained between 4 and 34 days after the estimated date of explosion (May 31.5 UT). These data cover a wide wavelength range from 2000 Å in the ultraviolet (UV) to 2.4 μm in the near-infrared (NIR). NIR spectra reveal helium in the atmosphere 3 days before the B-band maximum (B-max) and confirm the classification of SN 2011dh as a Type IIb. Optical spectra provide line profiles and velocity measurements of H I, He I, Ca II and Fe II to trace composition and kinematics of the supernova. UV spectra obtained with the Space Telescope Imaging Spectrograph show that the UV flux for SN 2011dh is low compared to other SN IIb. H I features are strong early and weaken during the period of our observations. He I features are first detected eleven days after the explosion and become progressively stronger. For all phases at which He is detected, the hydrogen line-forming region is separated from the helium layer by about 4000 km s^{-1}. This velocity gap is consistent with a H-rich shell surrounding the progenitor and we estimate the shell mass for SN 2011dh relative to other SN IIb. Both H I and He I maintain a constant velocity after B-max while Ca II and Fe II velocities continue to decline. Light curves are presented for twelve passbands: *UVW2,UVM2,UVW1,U,u',B,V,r',i',J,H and K*. SN 2011dh reached a maximum bolometric luminosity of $1.7 \pm 0.2 \times 10^{42}$ erg s^{-1}, about 23 days after the explosion. NIR emission contributes more than 35% of the total bolometric flux while the UV contribution is negligible. Peak brightness in the B-band was 13.17 mag on day 18.7 ± 0.5. We compare our results to other studies of SN 2011dh and to other Type IIb SN. We find that SN IIb with different masses for the H shell have similar peak luminosities, decline rates and colors from the time of maximum. That suggests that the progenitors inside of the H shells are close to the same composition and mass. These data will provide firm constraints for models of SN 2011dh based on the explosion of a yellow supergiant.

Subject headings: supernovae: general — supernovae: individual (2011dh) — Infrared: general — Ultraviolet: general

[1] Harvard-Smithsonian Center for Astrophysics, 60 Garden St., Cambridge, MA 02138, USA
[2] University of Texas at Austin, 1 University Station C1400, Austin, TX, 78712-0259, USA
[3] Department of Optics and Quantum Electronics, University of Szeged, Domter 9, 6720, Szeged, Hungary
[4] Clay Fellow. Harvard-Smithsonian Center for Astrophysics
[5] Department of Astronomy, University of California, Berkeley, CA 94720-3411, USA
[6] Astronomy Department, University of Virginia, Charlottesville, VA 22904, USA
[7] Department of Astronomy & Astrophysics, Pennsylvania State University, 525 Davey Laboratory, University Park, PA 16802, USA
[8] National Optical Astronomy Observatory, Tucson, AZ 85719, USA
[9] Center for Astrophysics & Space Astronomy, University of Colorado, 389 UCB, Boulder, CO 80309, USA
[10] Department of Astronomy, The Oskar Klein Centre, Stockholm University, S-106 91 Stockholm, Sweden
[11] Department of Physics, University of Notre Dame, 225 Nieuwland Science Hall, Notre Dame, IN, 46556, USA
[12] European Southern Observatory, 85748 Garching bei München, Germany
[13] University of Arizona, Steward Observatory, Tucson, Arizona 85721, USA
[14] Departamento de Ciencias Fisicas, Universidad Andres Bello, Avda. Republica 252, Santiago, Chile

1. INTRODUCTION

SN 2011dh (= PTF11eon) was discovered in the nearby "Whirlpool" galaxy M 51 ($D \approx 8.05$ Mpc). The time of explosion is constrained by the last reported non-detection by the Palomar Transient Factory on May 31.275 (Arcavi et al. 2011) and the earliest reported observation of SN 2011dh by A. Riou on May 31.893 (Reiland et al. 2011). The early detection and close proximity of SN 2011dh provide optimal conditions for detailed observations of the supernova.

Core-collapse supernovae are classified by type according to their observational characteristics. Type II SN are hydrogen rich and their spectra display prominent Balmer series features. SN Ib have helium features in their spectra but they lack hydrogen. The spectra of SN Ic do not have features of either hydrogen or helium. This sequence is interpreted as evidence for progressive stripping of hydrogen and helium from the outer atmosphere of the progenitor star, either by stellar winds or through mass transfer to a companion star. SN Ib and SN Ic are referred to as stripped-envelope core-collapse (SECC) events.

Type IIb supernovae form a separate class. They display strong hydrogen features in the early spectra but helium features are absent. Within a few weeks the H features weaken and are no longer detected while He features appear after about two weeks and progressively strengthen. The weakness of H features in SN IIb suggests that they are related to the SECC group. SN IIb have been proposed as an intermediate step between SN II and SN Ib (Filippenko, Matheson & Ho 1993; Nomoto et al. 1993; Woosley et al. 1994). For a review of the relationship between SN classifications and progenitor structure, see Nomoto, Iwamoto, & Suzuki (1995).

There are two proposed progenitor channels for SN IIb: an isolated star ($\gtrsim$ 25 $M_\odot$) that loses most of its hydrogen envelope through stellar winds (e.g., Chiosi & Maeder 1986) or a close binary system where mass transfer strips most of the hydrogen from the outer layers of the progenitor star (e.g., Podsiadlowski et al. 1993). The mass-transfer model requires a more compact progenitor, similar in size to a Wolf-Rayet star. SN IIb from compact progenitors display relatively weak early emission from the shock heated atmosphere and the thermal powered luminosity declines rapidly (a few days) after the explosion (Chevalier & Soderberg 2010). SN IIb with a massive hydrogen envelopes have extended cooling times such as ∼20 days observed for SN IIb 1993J.

The immediate post-explosion luminosity of Type IIb supernovae (the thermal peak) is produced by a hot atmosphere that has been heated by the shock from the explosion. The initial brightness fades rapidly as the shocked atmosphere cools. Radioactivity in the SN core powers a second increase in luminosity and the light curve rises to a new peak a few weeks after the explosion. The thermal peak, decline to a minimum and subsequent rise to a second maximum have been observed in the light curves of SN IIb 1993J (Schmidt et al. 1993; Wheeler et al. 1993; Lewis et al. 1994; Richmond et al. 1994, 1996), SN IIb 2008ax (Pastorello et al. 2008; Roming et al. 2009; Chornock et al. 2011; Taubenberger et al. 2011), SN IIb 2011fu (Kumar et al. 2013), and the peculiar SN II 1987A (Arnett et al. 1989).

A steep decline in the brightness of SN 2011dh is reported from day 1 to day 3 which is consistent with the cooling of the shocked atmosphere (Maund et al. 2011; Arcavi et al. 2011; Bersten et al. 2012; Tsvetkov et al. 2012). Our sample begins at day 4 and coincides with the time of B-band minimum between peaks. We present ultraviolet (UV), optical, and near-infrared (NIR) photometry from twelve filters and construct a bolometric light curve (LC) that describes the rise of the radioactive luminosity, the bolometric peak and the decline from maximum. We find a maximum bolometric luminosity for SN 2011dh of $1.7 \pm 0.2 \times 10^{42}$ erg s^{-1} that occurred about 23 days after the explosion. NIR photometry shows that the flux beyond 1 μm is about 35% of the bolometric flux before maximum and increases to more than 50% at day 34. The UV contribution to the bolometric luminosity for SN 2011dh is negligible.

We compare our results to the bolometric LC for SN 2011dh reported by Bersten et al. (2012) as well as the bolometric light curves of Type IIb SN 1993J and 2008ax. We find remarkable similarities among these three supernovae in the shape and luminosity of the light curves from 10–34 days after the explosion.

The first spectrum of SN 2011dh was obtained by Silverman et al. (2011) less than three days after discovery. The presence of strong Balmer lines and the absence of helium led them to classify SN 2011dh as a SN II. Optical spectra were obtained by Maund et al. (2011) and Arcavi et al. (2011) soon after and they both noted similarities between the early spectra of SN 2011dh and Type IIb SN 1993J without identifying He features. Marion et al. (2011) confirmed the Type IIb classification with the first detection of He I lines that we identified in NIR spectra obtained 16 days after the explosion (≈ 3 days prior to the B-band peak). The final version of Maund et al. (2011) identifies He I lines in optical spectra at 20, 30 and 40 days after the explosion. They report that the transition from H dominated spectra to He is nearly complete 40 days after the explosion.

We use NIR spectra obtained 8, 12, and 16 days after the explosion to explore the emergence of He I in the spectra and to compare the development of He I features with changes observed in the H I features. We show that He I begins to contribute to the spectra about 11 days after the explosion but blending prevents conclusive identification before day 16.

We measure velocities for absorption features of H I, He I, Fe II and Ca II and we search for evidence of other absorption features. Velocities for all lines decline through the time of B-max and then H I and He I velocities remain constant while Ca II and Fe II velocities continue to decline. A constant gap of about 4000 km s^{-1} is observed between the velocities of H I lines and He I lines. The separation of velocities is consistent with the presence of a low mass hydrogen shell on the progenitor. We use a simple model to estimate the mass of the shell surrounding SN 2011dh compared to other SN IIb.

Observations with the Space Telescope Imaging Spectrograph (STIS) spectrograph on the *Hubble Space Telescope* (*HST*) and the *Swift* U-grism provide rare UV spectroscopy of a SN IIb and extend the range of our spectroscopic analysis. SN 2011dh appears to have a UV deficit and we discuss the possible sources and implica-

tions.

The location of SN 2011dh was imaged by the *HST* in multiple filters prior to the explosion. Several groups identify a yellow supergiant star at the location of SN 2011dh and discuss whether this star is a plausible progenitor (Maund et al. 2011; Van Dyk et al. 2011; Murphy et al. 2011). Szczygiel et al. (2012) report that the star proposed as the progenitor was variable and had been fading for three years prior to the explosion at a rate that is unusual for similar stars in M 51.

Kochanek (2009) asserts that more than half of core-collapse SN will be in binary systems at the time of explosion. The possibility that SN 2011dh had a companion is explored by Maund et al. (2011); Van Dyk et al. (2011), and Murphy et al. (2011) with Van Dyk et al. (2011) concluding that the yellow supergiant is more likely to be a binary companion than the progenitor itself.

Bersten et al. (2012) construct hydrodynamical models for SN 2011dh and they conclude that the progenitor of SN 2011dh had an extended radius of at least $200R_{\odot}$ which is consistent with $R \approx 250R\odot$ for a F8I yellow supergiant. A complementary paper by Benvenuto, Bersten, & Nomoto (2013) describes binary evolution calculations that produce a YSG primary star, fit the model of Bersten et al. (2012) and match the star identified in pre-explosion *HST* images.

Other authors find evidence for a more compact progenitor. Soderberg et al. (2012) use optical, radio, and x-ray observations to suggest a compact progenitor radius of order $1R_{\odot}$. Prieto & Hornoch (2011) and Arcavi et al. (2011) cite the relatively short duration of the cooling phase as evidence for a compact progenitor. Krauss et al. (2012) with *EVLA* observations and Bietenholz et al. (2012) with *VLBI* data use radio emission and a synchrotron self-absorption model to support the compact nature of the progenitor.

Horesh et al. (2012) combine radio, millimeter, optical, and X-ray data to model the blast wave and find an intermediate shock velocity for SN 2011dh. Since the size of the progenitor is inversely proportional to the velocity of the shock (Chevalier & Soderberg 2010), the authors conclude that the pre-explosion radius of the SN 2011dh progenitor was between the radii of a "compact" star and a star with an extended envelope. They suggest that this result favors a continuum of sizes for SN IIb progenitors rather than a bimodal distribution consisting only of compact or extended stars.

Van Dyk et al. (2013) observed SN 2011dh with the *HST*/WFC3 almost 700 days after the explosion. They obtained evidence that the yellow supergiant star at the location of the SN has disappeared which suggests that it was correctly identified as the progenitor. Now that we know the identity of the star that exploded, theoretical explanations can focus on much more specific physical models. We hope that these detailed observations of SN 2011dh will guide the selection of correct models for this explosion, and lead to a better understanding of SN IIb.

The data acquisition and reduction details are presented in § 2. Spectral features and measured velocities are discussed in § 3. Synthetic spectra from SYNOW are used to confirm line identifications and to discuss physical properties in § 5. Multi-band light curves, color evolution and the SN temperature are presented and discussed in § 6. The bolometric light curve is described in § 7. A summary and conclusions are presented in § 8.

2. THE OBSERVATIONS

The Whirlpool Galaxy (M 51) is a lovely galaxy that is frequently imaged by professionals and amateurs. SN 2011dh was not detected in an image obtained by the Palomar Transient Factory (PTF) on May 31.275 to a limiting magnitude of $g = 21.44$. The first detection of SN 2011dh was by amateur A. Riou on May 31.893 (UT) and there were several independent discoveries soon thereafter (Reiland et al. 2011). The PTF also made an independent discovery on June 1.191 and many early sources reference the target using the name: PTF11eon. For this paper, we adopt an explosion date of May 31.5 UT (MJD 55712.5) and we express the times of all observations in days relative to the explosion. Uncertainties of a few hours for the time of t_0 do not affect the presentation of our results or our conclusions.

Distance measurements for M 51 have a significant scatter. Tonry et al. (2001) use surface brightness fluctuations (SBF) to determine $D = 7.7 \pm 0.9$ Mpc. However M 51 is a large spiral galaxy and there may be significant dust present that would compromise the effectiveness of the SBF method. The Tonry et al. (2001) result matches the value of $D = 7.7 \pm 1.3$ Mpc found in Nearby Galaxies Catalogue that was determined using the Tully-Fisher method (Tully 1988). A higher value for D is found by Vinkó et al. (2012) who use the expanding photosphere method (EPM) to measure the distance to M 51 as $D = 8.4 \pm 0.7$ Mpc. Feldmeier, Ciardullo, & Jacoby (1997) also measure $D = 8.4 \pm 0.6$ Mpc using a planetary nebula luminosity function.

For this paper, we adopt a value that is the mean of these four measurements ($D = 8.05$ Mpc). We note that the maximum difference of ± 0.35 Mpc between our adopted value for D and any of the referenced measurements introduces only ± 0.1 mag uncertainty in the luminosity measurements. Such a small difference has no significant effect on our results. We use a heliocentric velocity of 600 km s^{-1} (NED; Rush, Malkan, & Edelson (1996)) to correct wavelength measurements to the rest frame.

Extinction from the host is low. Vinkó et al. (2012) and Arcavi et al. (2011) do not detect Na D lines at the redshift of M 51 in high-resolution spectra. Arcavi et al. (2011) set an upper limit on extinction from the host at $E(B - V) < 0.05$ mag. Ritchey & Wallerstein (2012) identify weak absorption components from Na D and Ca II H&K in high-dispersion spectra but they conclude that the overall weakness of the Na D detection confirms a low foreground and host galaxy extinction. The *HST*/STIS spectrum in our sample shows interstellar Mg II (λ2795) absorption with an equivalent width of approximately 1 Å, which is consistent with the assumption of low extinction.

Galactic extinction is $E(B - V) = 0.035$ mag (Schlegel et al. 1998), which means that the V-band extinction correction is ≈ 0.1 mag. We correct for Milky Way extinction when constructing the bolometric luminosity but in the figures and tables we present the measured values.

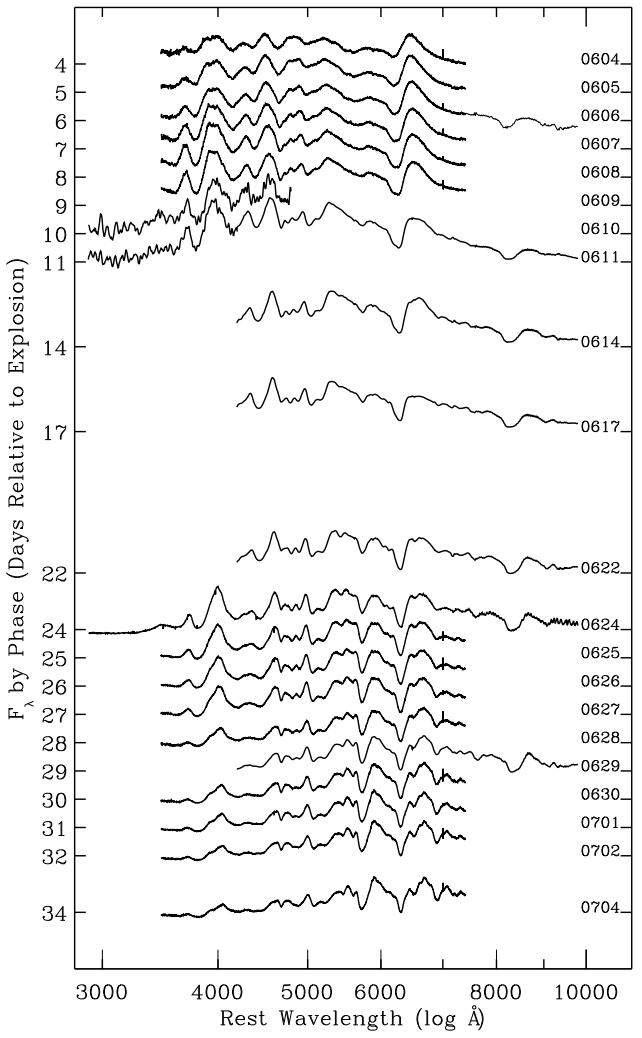

FIG. 1.— UV and Optical spectra from SN 2011dh were obtained with the *HST*/STIS (day 24, 2800–10000 Å), Tillinghast/FAST (3400–7400 Å), HET/LRS (4200-10000 Å) and *Swift*/U-grism (days 10 and 11, 2800–4600 Å). The spectra are positioned so the flux at 7500 Å aligns with the phase with respect to the explosion listed on the ordinate. The corresponding dates of observation are listed at the right. Spectral features are discussed in § 3. Observing details are listed in Table 1.

2.1. *Spectroscopy*

The observing details for twenty-six spectra of SN 2011dh obtained between 4 and 34 days after the explosion are given in Table 1. On some of the days two spectra were obtained that cover different wavelength regions. These spectra were combined to form a single spectrum for each phase.

Figure 1 shows twenty-one spectra of SN 2011dh from 2800–10000 Å. The sample includes optical spectra (3480–7420 Å) obtained at the F. L. Whipple Observatory (FLWO) 1.5-m Tillinghast telescope using the FAST spectrograph (Fabricant et al. 1998) on days 4–9, 24–28, 30–32, and 34 with respect to the time of explosion. FLWO/FAST data are reduced using a combination of standard IRAF and custom IDL procedures (Matheson et al. 2005). Additional optical spectra (4200–10100 Å) were obtained on days 6, 11, 14, 17, 22, and 29 with the 9.2m Hobby-Eberly Telescope

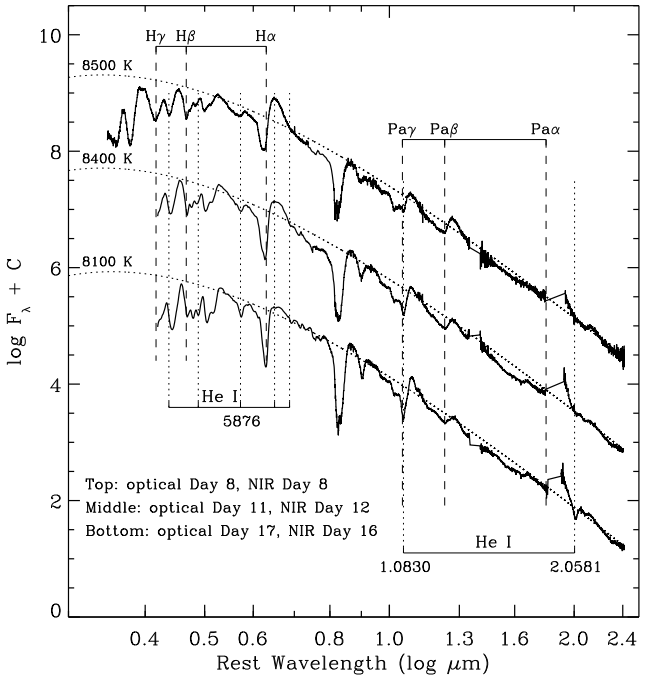

FIG. 2.— Optical and NIR spectra of SN 2011dh from 0.32–2.4 μm. Balmer and Paschen lines (α, β and γ) are marked at 12000 km s^{-1} and He I lines are marked at 8000 km s^{-1}. H I is strong at all phases displayed here. There is no He I detection on day 8 (top) and identification is inconclusive due to blending on days 11 and 12 (middle). He I is clearly detected on day 16 (bottom) in the NIR at $\lambda\lambda$1.0830, 2.0581 and in the optical at λ5876. The dotted lines are blackbody temperature curves as discussed in the text.

(HET; Ramsey et al. (1998)) at the McDonald Observatory using the Marcario Low-Resolution Spectrograph (Hill et al. 1998). HET/LRS spectra are reduced with standard IRAF procedures.

Low ($R \approx 200$, $\lambda = 0.65 - 2.5$ μm) and medium ($R \approx 1200$, $\lambda = 0.80 - 2.4$ μm) resolution NIR spectra were obtained on days 8, 12, and 16 with the 3 meter telescope at the NASA Infrared Telescope Facility (IRTF) using the SpeX medium-resolution spectrograph (Rayner et al. 2003). Figure 2 displays the NIR spectra with contemporaneous optical spectra. IRTF data are reduced using a package of IDL routines specifically designed for the reduction of SpeX data (Spextool v. 3.4; Cushing, Vacca, & Rayner (2004) 2004).

Low-resolution UV spectra were obtained by *Swift* with the UVOT U-grism (2000–4600 Å) on days 10 and 11. The data were downloaded from the *Swift* archive[15]. *Swift* data are analyzed within HEAsoft following the standard recipe in the "UVOT User's Guide."[16] The raw frames are converted into 'DET' images by applying the `swiftxform` task after flatfielding and bad-pixel masking. The final spectra are extracted and calibrated with the `uvotimgrism` task. Wavelength and flux calibrations are corrected by matching the U-grism spectra with contemporaneous ground-based spectra covering 3000–5000 Å.

A spectrum of SN 2011dh was obtained on day 24

[15] http://heasarc.gsfc.nasa.gov/docs/swift/archive/
[16] http://heasarc.gsfc.nasa.gov/docs/swift/analysis/UVOT_swguide_v2_2.pdf

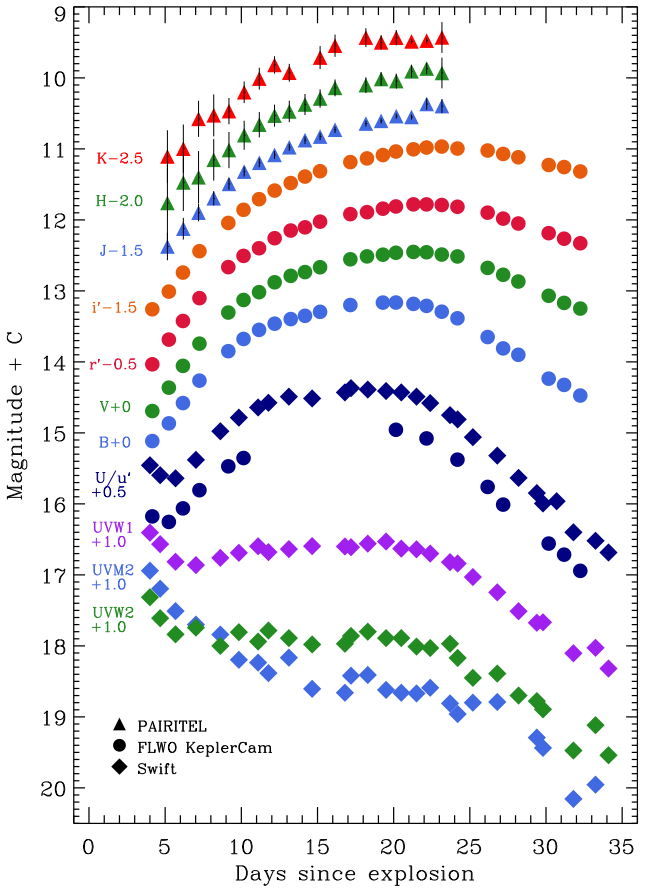

FIG. 3.— UVOIR photometry of SN 2011dh in 12 filters obtained on days 4–34 by the *Swift* satellite and FLWO telescopes KeplerCam and PAIRITEL. Uncertainties are smaller than the symbols used for plotting except where indicated for some of the PAIRITEL data. The *Swift* U-band and the KeplerCam u'-band are plotted with the same offset and the light curves are different by about 0.5 mag. We fit the data for each filter with a polynomial and list the peak magnitudes, dates of peak and the central wavelengths in Table 2. SN 2011dh had not reached maximum in the NIR before the final JHK_s observations on day 24 but all NIR light curves appear to be within a day or two of peak.

with STIS on the *HST* under observing program GO-12540 (PI: R. P. Kirshner). Three STIS gratings were employed with the CCD detector: G230LB (3600 sec), G430L (800 sec), and G750L (350 sec) and the combined spectrum covers 2160–10230 Å. The *HST* data are reduced using the STScI STIS pipeline.

2.2. *Photometry*

Photometry of SN 2011dh was obtained in twelve filters and the light curves are displayed in Figure 3. Table 2 gives the peak magnitudes and dates of peak for each passband. The values were determined by fitting a second order polynomial to the data. The central wavelengths for each filter are also in the table.

SN 2011dh was observed at the FLWO with the 1.2-m telescope and the KeplerCam instrument in the *uBVri* bands (Table 3). The KeplerCam data are reduced using IRAF and IDL procedures as described in Hicken et al. (2007) and they are converted to the *u'BVr'i'* standard-system following the methods described in Hicken et al. (2012). These data have not been s-corrected and no host-galaxy subtraction was performed since the SN was well separated from the galaxy center and other stars.

NIR images were obtained in the J, H, K_s bands by the Peters Automated Infrared Imaging Telescope (PAIRITEL), a 1.3-m $f/13.5$ telescope located at the FLWO (Table 4). The data are processed into mosaics using the PAIRITEL Mosaic Pipeline version 3.6 implemented in python. Details of PAIRITEL observations and reduction of supernova data can be found in Friedman (2012).

UVOT photometric data were downloaded from the *Swift* archive (Table 5). *Swift* photometry is reduced with HEAsoft following standard procedures. Individual frames were summed with the `uvotimsum` task, and magnitudes were determined via aperture photometry using the task `uvotsource` with a 5 arcsec radius aperture. This sequence produces standard Johnson magnitudes in *UBV* filters, and flight-system magnitudes in *UVW2, UVM2* and *UVW1*. The transmission profiles of the *UVW1* and *UVW2* filters have extended red wings that permit flux contributions from beyond the intended wavelength regions.

3. THE SPECTRA

Figure 1 displays twenty-one optical spectra of SN 2011dh. The earliest spectrum in our sample was obtained on June 4.2 UT which is estimated to be less than four days after the explosion. The last spectrum was obtained on July 4 which is 34 days after the explosion. Observing details for each spectrum are given in Table 1.

The wavelengths of lines, features or spectra are expressed in Angstroms for wavelengths less than 8000 Å and in microns for wavelengths greater than or equal to 0.80 μm. For discussions of wavelength ranges that cross 8000 Å, as in the following paragraph, both wavelengths are described with the same units. Observation times are expressed in whole days relative to the explosion. For another point of reference, the B-band maximum occurred about 19 days after the explosion.

Figure 2 displays pre-maximum optical and NIR spectra from SN 2011dh covering the wavelength region 0.32–2.40 μm. The NIR data were obtained at the IRTF with SpeX on days 8, 12, and 16 while the corresponding optical data were obtained at the FLWO with FAST on day 8 and the HET with LRS on days 11 and 17.

The Balmer and Paschen series of hydrogen lines are clearly detected and the α, β, γ lines from both series are marked at positions corresponding to a blue shift of 12000 km s^{-1}. This velocity is a good representation for H I on day 16 (bottom) and helps locate the H I features at other phases when the velocities are higher. All of the H features remain strong throughout the time covered by this figure.

He I lines are marked in Figure 2 at 8000 km s^{-1}. Eight days after the explosion (the top spectrum) no He I features are detected. At 11 and 12 days (middle), weak contributions are probable from He I $\lambda\lambda$5876,1.0830 to blended absorption features that are dominated by Na I λ5892 and Paγ λ1.2818 respectively. The spectra obtained on days 16 and 17 reveal unambiguous features of He I from λ5876 and both strong NIR lines ($\lambda\lambda$ 1.0830,2.0581). The appearance of He I and other significant features in these spectra are discussed in the following subsections.

Blackbody (BB) temperature curves are plotted as dot-

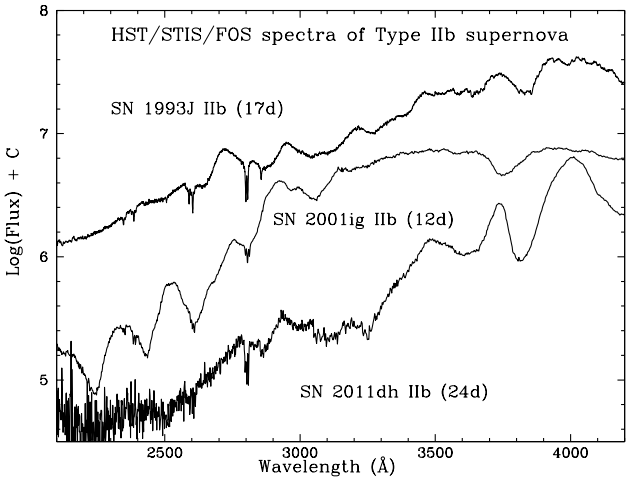

FIG. 4.— *HST*/STIS data from three Type IIb SN. The spectra are displayed from 2000–4200 Å to show detail in the UV region. The SN 2011dh spectrum obtained on day 24 (bottom) reveals a reduced UV flux at wavelengths less than 3300 Å compared to spectra from SN IIb 2001ig at day 12 (middle) and SN IIb 1993J at day 17 (top). We model this region with SYNOW (§ 5) and the results suggest that the UV suppression is due to line-blanketing from Ti II and Co II.

ted lines in Figure 2. The observed shapes of the OIR continua are fit best by BB curves for 8500 K at 8 days, 8400 K at 12 days, and 8100 K at 16 days. A more detailed discussion of temperature estimates can be found in § 7.1.

Figure 1 shows that the *HST*/STIS spectrum obtained on day 24 extends from 2100–10000 Å, though the portion beyond 9000 Å suffers from fringing. At other phases it is necessary to combine 2 or 3 spectra from other sources to cover this range. Features of Ca II H&K λ3945 and the Ca II infrared triplet λ8579 are both observed in a single spectrum. The optical portion of the STIS spectrum is in good accord with a FAST spectrum obtained on the same date and with the HET spectrum obtained on day 22.

One unique part of this spectrum is the high-quality UV coverage. Figure 4 shows the 2000–4200 Å region of the *HST*/STIS spectrum from SN 2011dh on day 24, plotted with STIS spectra of SN IIb 1993J (Jeffery et al. 1994) and 2001ig at comparable phases. The flux from SN 2011dh is clearly suppressed below 3300 Å relative to the other SN IIb. Fe II, Ti II, and Cr II are expected to be strong contributors to the UV spectrum and these lines can create a line-blanketing effect that shifts flux from the UV to longer wavelengths. In § 5 we analyze the UV region of this spectrum using model spectra from SYNOW. The spectrum of SN 2001ig is from the HST archives and has not been previously published.

3.1. *Hydrogen Features*

Silverman et al. (2011) reported that a Keck I+LRIS spectrum of SN 2011dh obtained on day 3 revealed P Cygni profiles for hydrogen lines that are characteristic of Type II supernovae. The data in our sample begin the following day and prominent H I lines from the Balmer and Paschen series are evident in the early spectra.

Figure 5 displays features from Hα, Hβ, Hγ and Paβ by phase in velocity space. H I features are strong in the

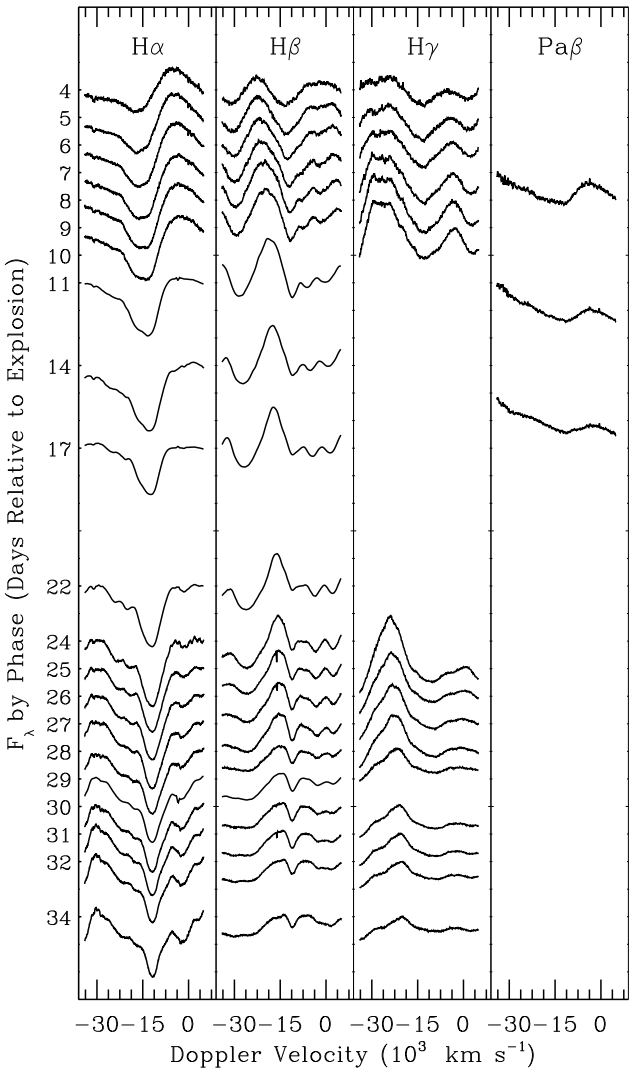

FIG. 5.— Hydrogen features in velocity space. Hα velocities are 15400 km s^{-1} on day 4 and decline to about 12500 km s^{-1} on day 14. From day 14 to 34 Hα velocities remain nearly constant at about 12000 km s^{-1}. All H I features are strong is the earliest spectra and they become weaker and narrower with time. Hα appears to be formed by 2 separate components on days 4–17. Hβ is distorted and pushed to lower velocities. Paβ (right panel) is less blended than the Balmer series lines and it clearly demonstrates that the H I absorption weakens from day 8–16. The continuum of each segment is aligned with the phase listed on the ordinate. Flux values for Paβ are multiplied by 5 to facilitate comparison. Velocities are listed in Table 6.

first week after the explosion and then they become progressively weaker and narrower with time. Hα is the only H I line that continues to form a significant absorption 34 days after the explosion. Maund et al. (2011) report that the transition from H dominated spectra to He is nearly complete 40 days after the explosion.

Hα velocities decline from 15400 km s^{-1} on day 4 to 12500 km s^{-1} on day 14. For the next week, the velocities decline slowly to 12100 km s^{-1} on day 22. After that, Hα velocities do not vary from 12000 km s^{-1} by more than 100 km s^{-1}. Hβ follows the shape of the Hα velocity curve with with values about 1500 km s^{-1} less than Hα velocities except from day 11 to day 17 when the separation is about 2000 km s^{-1}.

In the first two weeks after the explosion, Hα line

profiles show evidence for two separate absorption components. The Hα absorption feature in the day four spectrum can be fit by two gaussians with minima that correspond to velocities of 17300 and 15400 km s^{-1}. Silverman et al. (2011) reported the Hα velocity on day 3 to be 17600 km s^{-1} which suggests that they measured the blue component. Comparing the Hα features by phase shows that the component on the red side of the double bottom becomes dominant after day 8 and by day 24 the features no longer have two minima. For consistency, we measure Hα velocities using the red component at all phases.

The source of the blue component in the Hα features is ambiguous. One possibility is a second H-rich region at about 2000 km s^{-1} higher velocity. The outer H layer could be created by interaction with circumstellar material (Chugai, Chevalier & Utrobin 2007). No comparable high-velocity (HV) components are found in the absorption features from other H I lines, but they could be disguised by blending. SYNOW models suggest this is a possibility. The addition of a second H region to SYNOW models can fit the observed "double" Hα line profiles without producing strong HV features for other H I lines.

Si II λ6355 could also be the source of the blue absorption component in these features, but that identification requires the Si II velocities to be 5000 km s^{-1} lower than Ca II and 4000 km s^{-1} lower than Fe II at these early phases. SYNOW models can also produce features that match the Hα line profiles using Si II for the blue component.

Figure 5 shows that line profiles for most H I features are distorted by the influence of nearby lines beginning about one week after the explosion. Features from the other lines are gaining strength through the time covered by our observations while H I is fading.

The emission component of Hα is flattened by He I λ6678 beginning about day 11 and Si II λ6355 may affect the absorption component.

Hβ is distorted on the red side by P Cygni emission from a strong blend of Mg II λ4481 and Fe II λ4561. Figure 5 shows how the Hβ feature is shoved to longer wavelengths which results in lower measured velocities for Hβ. After maximum brightness, He I λ4492 produces the same effect on Hβ. Table 6 shows that the measured velocities for Hβ are $\approx$ 1500 km s^{-1} less than Hα at all phases except from day 11 to day 17 when Hβ velocities are $\approx$ 2000 km s^{-1} lower.

Hγ is squeezed by Ca II H&K emission on the blue side and by the Mg II λ4481 and Fe II λ4561 feature on the red side. Our data do not cover the Hγ region between days 11–24 and it is not possible to identify Hγ after that.

Figure 2 shows that Paα λ1.8751 is located in a region of almost complete atmospheric opacity. We follow standard practice for displaying NIR spectra and omit the very noisy regions (1.32–1.38 μm and 1.79–1.88 μm) where the atmospheric transmission is less than 50%. After these data have been removed only the tail of the emission component for Paα remains visible.

The H I line that is most free from blending is Paβ λ1.2818. Features from this line are displayed in the rightmost panel of Figure 5 and they show that the strength of the H I signal is clearly diminishing from day 8 through day 16. Unfortunately our NIR spectra cover only a limited range of dates.

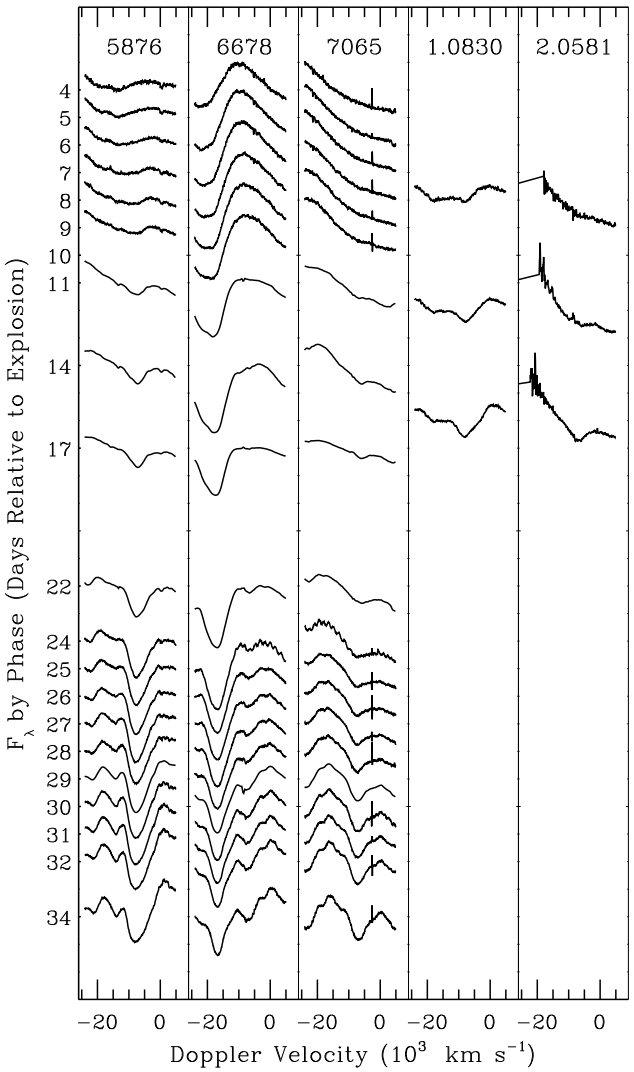

FIG. 6.— He I features in velocity space. Helium is not detected for at least 10 days after the explosion. Marginal detections are made on day 11 for He I λ5876 and day 12 for λ1.0830 but both features are significantly blended by Na D and Paγ respectively (see also Figure 2). At 16 days after the explosion He I is clearly detected from both NIR lines $\lambda\lambda$1.0830,2.0581 and the optical line λ5876. He I features progressively strengthen through the time covered by these observations and velocities are nearly constant from day 14 to day 34. The continuum of each segment is aligned with the phase listed on the ordinate. Flux for the λ2.0581 feature is multiplied by 10 to facilitate comparison. Velocities are listed in Table 6.

3.2. *Helium Features*

The presence of helium in their spectra differentiates SN IIb from other Type II SN but classification is only one reason to search for helium. Early detection and detailed measurement of He I features will help explain the physical reasons for the transition in SN IIb from a hydrogen dominated epoch soon after the explosion to the later phases dominated by helium.

Figure 6 displays features for three optical and two NIR He I lines by phase in velocity space. He is not detected through at least day 11. There are tentative identifi-

cations at days 11 and 12 but conclusive evidence for He I does not appear until day 16. He I features become deeper and broader though the end of our observations on day 34.

NIR spectra provide the most reliable detections of He I features in early observations of SN because optical He I lines are weaker or blended. Figures 2 and 6 show that He I lines at optical wavelengths are difficult to identify in the early data (see also the discussion of He I lines in SN 2008ax by Chornock et al. (2011)).

The strongest optical He I line is λ5876 and it may begin to form an absorption feature as early as day 11. But there is also a strong presence of Na D and there are no other He I features detected in optical spectra until day 24. Identification of He I with optical data alone is uncertain at this phase. A simultaneous detection of more than one line is required to securely identify He I.

With NIR spectra it can be misleading to base identification of He I on the λ1.0830 line in isolation (beside the fact that it violates the admonition in the previous paragraph). The broad absorption feature from about 1.02–1.06 μm is found at this location in the spectra of most core-collapse SN, including SN Ic that never display He I. Paγ λ1.0938, He I λ1.0830 and Fe II λ1.0500 are usually the most prominent contributors to this feature but it can be difficult to define specific minima and associate them with individual lines. Several other strong lines are found in this region and a combination of them is likely to help form the line-profile. Good candidates include: C I λ1.0603, Mg II λ1.0927, Si I $\lambda\lambda$1.0608,1.0962, S I λ1.0457, Fe II λ1.0863 and Ti II λ1.0691.

H I lines in Figure 2 are marked at 12000 km s^{-1} and He I lines are marked at 8000 km s^{-1} which corresponds day 16 velocities. This difference in the blueshift of these lines places the expected absorption minima for Paγ and He I λ1.0830 within 100 km s^{-1} of each other. The source of the absorption found at the blue end of this feature, about 9500 km s^{-1} from Paγ and He I λ1.0830, is Fe II λ1.0500. Paγ dominates the red component of the 1.02–1.06 μm feature on day 8 and all H I lines are strong at this phase. On day 12, the red end of the feature has developed more of a P Cygni profile that is probably due to He I λ1.0830 but the influence of Paγ remains strong. At this phase He I λ2.0581 produces only a weak, ambiguous signal, and does not provide a confirming detection.

On day 16, both He I lines $\lambda\lambda$1.0830,2.0581 can easily be identified in the NIR spectrum (Marion et al. 2011). The absorption feature for He I λ2.0581 is pushed to the red by the strong emission component of the Paα P Cygni profile that is mostly hidden in the high opacity region that we omit from the spectra. The optical He I λ5876 line becomes clearly defined at the same phase but no other He I lines are detected at optical wavelengths until day 24 (Figure 6).

Other He I lines begin to emerge about day 17 which is near the time of B-max. In the early spectra He I λ3889 is blended or obscured by Ca II H&K and Si II λ3858. After B-max, He I λ3889 is strong enough to distort the Ca II H&K feature by extending it on the blue side, but accurate measurement of He I contribution is not possible. He I λ4492 is blended with Fe II λ4561 and Mg II λ4481 and it is not possible to unravel the He I contribution from the blend. He I λ5016 is blended with Fe II λ5018 at all phases covered by these data. He I λ6678 begins to flatten the emission component of Hα on day 14 but contributions from this line are obscured by Hα emission until 22 days after the explosion.

Features from He I $\lambda\lambda$5876,6678,7065 become increasingly obvious after B-max. He I λ7065 is weakly present in spectra from days 14 and 17 and because this line is relatively unblended it provides a reliable benchmark for He I velocities at all phases. Table 6 shows that the velocities for all He I lines are within 1000 km s^{-1} of He I λ7065 after He I has become established.

3.3. *Ca II and Fe II Features*

We search the spectra of SN 2011dh for evidence of features from ions other than H I and He I. The only unambiguous identifications are made for Ca II and Fe II. We discuss the characteristics of features from individual lines and how they may influence the measurements.

Ca II— is clearly detected from both the infrared triplet (IR3, λ0.8579) and Ca II H&K (λ3945). These strong lines create broad absorption features with rounded bottoms which makes them more difficult to measure than features with narrow and distinct absorption minima. The Ca II features do not appear to have separate contributions from two or more lines as found in the early Hα features. To make the measurements we define a straight line continuum between the flux at specific wavelengths on both sides of each feature. With this line profile small changes in the position of the assumed continua due to noise or imperfect telluric removals can create differences up to 2000 km s^{-1} in the positions of the minima of these features. Consequently velocity uncertainties for Ca II are greater than for velocities measured from narrow features. By using a consistent measurement technique we provide a satisfactory description of the behavior of Ca II velocities in the spectra from SN 2011dh.

On day 6 and day 11, the IR3 profile is similar to the combined profile of high-velocity (HV) and photospheric Ca II that is often seen in early spectra from Type Ia supernovae (Mazzali et al. 2005). But it is not possible to clearly define separate minima in the IR3 feature and Ca II H&K displays no evidence for a HV component at these epochs. After day 17 the profile of the Ca II IR3 feature becomes asymmetrical with the blue side a steeper gradient than the red side.

The Ca II H&K feature becomes stronger from the first observation on day 4 through day 11. This is followed by a gap in our coverage of this wavelength region from day 12 to day 23. On day 24 Ca II H&K is still strong but the feature declines after day 27 and is very weak by day 34. Ca II H&K is likely to be blended with Si II λ3858 and He I λ3889.

Fe II— becomes stronger from the earliest observations through day 14 and then slowly declines. The λ5169 line is most frequently used to represent Fe II velocity in SN IIb (Taubenberger et al. 2011). An absorption feature from this line is detected in all optical spectra in our sample. Unlike H I and He I for which the velocity remains nearly constant after day 17, the Fe II velocity steadily declines through the entire time period covered by our observations. Fe II λ4561 blends with Mg II λ4481 to create a strong absorption feature in the early spectra. This feature becomes stronger but even less defined

when He I λ4492 begins to contribute after day 17. Fe II λ5018 is distinct on days 4–14. This line is subsequently blended with He I λ5016 and eventually obscured as the helium lines become stronger. Fe II λ1.0500 is present and measured in all of the NIR spectra.

3.4. *Other Features*

The following ions show hints of absorption features from some of their stronger lines. We discuss the most likely identifications.

O I— is not detected through day 17 but may be emerging in the day 22 and 29 spectra from the λ7773 O I line. The absorption feature found near 0.90 μm in the NIR spectra on days 8, 12, and 16 is not primarily due to O I λ0.9264 because the stronger O I λ7773 line is not detected before day 22.

Mg II— is likely to be present in the NIR spectra from the λ0.9227 line that contributes to the strong absorption near 0.9 μm in a blend with O I λ0.9264 and Si II λ0.9413. Mg II λ1.0927 is a part of the broad absorption feature from 1.01– 1.06 μm but no individual lines are identified in this blend other than Paγ, He I λ1.0830 and Fe II λ1.0500. Mg II λ4481 definitely contributes to the absorption feature found near 4350 Å in a blend with Fe II λ4561. The minimum of this feature corresponds to less than 7000 km s^{-1} for Mg II which is inconsistent with the velocities of other intermediate mass elements. This suggests that the 4350 Å absorption feature is dominated by Fe II early and He I λ4492 after day 17.

Si II— does not produce obvious absorption features. Si II λ6355 may contribute to the Hα double feature (§ 3.1). However the minima of the blue components correspond to Si II λ6355 velocities of 8500 km s^{-1} on day 4 and less than 8000 km s^{-1} on days 8–10. Those velocities are more than 4000 km s^{-1} less than any other lines measured during these phases. Si II λ3858 may influence the blue side of the Ca II H&K feature but detection is not possible. Si II λ4130 is a candidate for the flat top and slight absorption in the Ca II H&K emission component found near 3950 Å in the early spectra. But the velocities required are greater than observed for Hα. In the NIR, Si II λ0.9413 may contribute to the 0.9 μm feature in a blend with Mg II λ0.9227. The small absorption features in the *H*-band at about 1.65 μm on days 12 and 16 could be from Si II λ1.6930.

Ti II and Co II— are the likely source of the steep drop of the continuum flux below 3300 Å due to line blanketing (Figure 4). Unlike SN 2001ig, there are no distinct absorption features in this region that can be associated with individual lines but SYNOW model spectra (§ 5) require significant contributions from Ti II and Co II to match the reduction of the UV-continuum level observed in early spectra from SN 2011dh.

4. THE VELOCITY MEASUREMENTS

Velocity measurements for H I, He I, Ca II and Fe II are plotted by phase in Figure 7 and in listed Tables 6 and 7. The velocities of H I, Ca II and Fe II decline by about 2500 km s^{-1} from the initial observations on day 4 to day 11 when the first evidence for He I appears. A much lower rate of decline is observed after day 11. No data were obtained from 18 to 21 days after the explosion, the *B*-band maximum occurs on day 19 and the bolometric maximum is on day 23. When the data resume on day 22, H I and He I velocities remain constant while the velocities for Fe II and Ca II continue to decline.

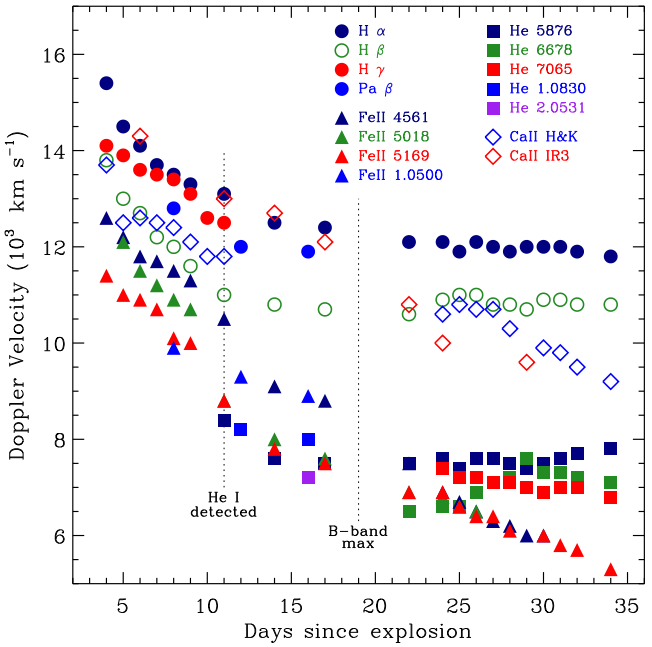

FIG. 7.— Velocities of H I, He I, Ca II, and Fe II plotted by phase. All velocities decline rapidly until about day 11 when He I is first detected. The velocity gradient for H I and Ca II is much lower from day 11 through maximum while He I and Fe II velocities continue decline at the same rate. After maximum, H I and He I velocities remain constant while Ca II and Fe II continue to decline. The gap between the H I velocities (circles) and He I velocities (squares) is nearly the same at all phases. Open symbols indicate features for which there is increased uncertainty in the velocity measurements (see § 3.2 and 3.3). Values used in the figure are listed in Tables 6 and 7.

Figure 7 graphically illustrates the consistent separation between the H I velocities (circles) and the He I velocities (squares). The different lines are plotted with different colors. Hα (dark blue, filled circles) is found at 15400 km s^{-1} on day 4 and after day 17 Hα velocities are nearly constant at $\approx$ 12000 km s^{-1}. Hβ velocities are lower than Hα at all phases due to the influence of other features (§ 3.1). The Hβ measurements are plotted with open circles (green) to represent increased uncertainties due to this distortion. Hγ velocities (red, filled circles) are close to Hα velocities on days 5–10. Paβ velocities (medium blue, filled circles) are only available for the three phases at which NIR data were obtained and they are consistent with the velocities of Hα and Hγ.

He I velocites are plotted in Figure 7 with filled squares. The marginal detections for He I $\lambda\lambda$5876,1.0830 on days 11 and 12 (§ 3.2) are included in the figure. The decline in He I velocity from day 11 to day 16 is consistent with other measured lines in that period. The He I features strong enough to be measured before day 22 are formed by the optical λ5876 line (dark blue) and NIR lines at $\lambda\lambda$1.0830,2.0581 (medium blue, purple). From day 22 through the end of the data, velocities for the optical He I lines are offset slightly from each other due to distortion from other features but each line maintains a nearly constant velocity.

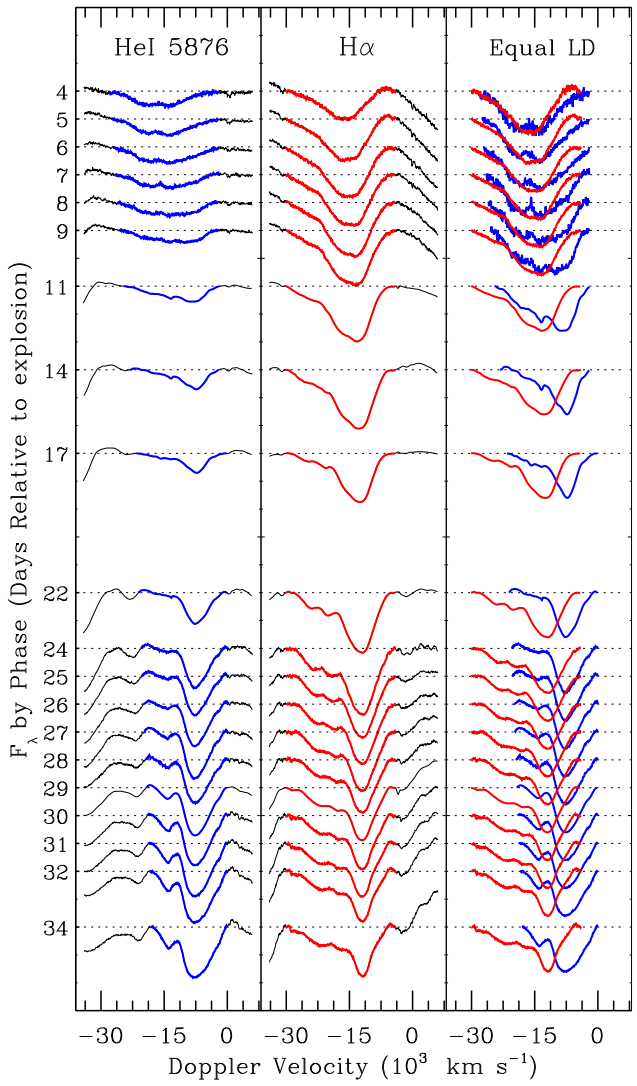

FIG. 8.— He I λ5896 (blue) and Hα (red) normalized to a flat continuum and plotted in velocity space. The left and center panels have the same relative flux scaling. He I is absent or very weak and blended with Na D prior to the first marginal detection on day 11. He I becomes progressively stronger through the end of our data. Hα appears to have two components on days 4–14. Hα and all H I features get weaker and narrower from day 17 to 34. The right panel shows the features plotted together with line depths normalized to the same value. By the time He I develops a clearly defined minimum at day 14, the H I and He I velocities are separated by about 4000 km s^{-1}. The velocities and separation remain essentially constant from day 14 to day 34.

Ca II velocities are marked with open diamonds in Figure 7 to reflect a higher level of uncertainty due to the broad line profiles (§ 3.3). Ca II IR3 velocities show an almost linear decline from day 6 to day 29. Velocities for the Ca II IR-triplet and Ca II H&K lines are separated by $\approx$ 1500 km s^{-1} from day 6 to day 11 with IR3 velocities similar to Hα and H&K velocities similar to Hβ. From day 22 through day 34, Ca II velocities for both features are similar and together they move away from the H-layer velocities toward the He-layer velocities.

Fe II velocities (filled triangles) decrease at a nearly constant rate throughout the entire period covered by these observations except for an abrupt drop from about day 9 to day 12. This may be due to an opacity effect because it occurs at about the same time that we begin to see evidence for He I. After day 22, Fe II velocities do not become constant, like H I and He I, but they continue to decline through the end of our observations. Figure 7 shows that Fe II velocities separate from H I velocities about two weeks earlier than Ca II velocities make the same transition.

The velocity patterns found in SN 2011dh are similar to those reported for SN 2008ax by Taubenberger et al. (2011). The shared characteristics include the relative velocities of H I, He I Fe II, and Ca II, the magnitude of the velocity gap between H and He, the velocities for H and He becoming constant and the lack of a velocity plateau for Ca II and Fe II.

4.1. *Separate Line-Forming Regions for H and He*

Throughout the text we describe the velocity gap between the H and He regions as "about 4000 km s^{-1}". We use that value to approximate the mean separation between H I and He I velocities. Table 6 shows that the actual range of separations is 3600–4600 km s^{-1} when the variations we attribute to the influence of other features are included. The separation between Hα and He I λ5876, which are the strongest lines from each region, is $\approx$ 4400 km s^{-1}. Inspection of the plotted data shows that the gap between H I velocities and He I velocities is consistent with a characterization of "$\approx$ 4000 km s^{-1}."

Figure 7 illustrates that H I and He I velocities maintain a nearly constant separation from first detection of He I though the last phase covered by our sample. The measured velocities for individual lines may be reduced due to the influence of adjacent lines (§ 3.1, 3.2) but the velocity differences between lines is nearly constant at all phases so that the plotted velocities for all H I and He I lines are essentially parallel.

Hβ follows the shape of the Hα velocity curve with with values about 1500 km s^{-1} less than Hα velocities except from day 11 to day 17 when the separation is about 2000 km s^{-1}. Velocities for He I $\lambda\lambda$6678,7065 are consistently 500–1000 km s^{-1} lower than He I λ5876.

Figure 8 presents another way to view the velocity relationship between the H and He regions. He I λ5876 (left column, blue) and Hα (center, red) are plotted by phase and in velocity space with the same relative flux scale. He I is absent or very weak in the early data and it is blended with Na D. The earliest tentative detection of He I is on day 11 (§ 3.2). The figure shows that from the time of He I detection, He I features become progressively stronger while H I features weaken.

The right panel shows the H I and He I features plotted together with the line depths normalized to the same value. Generally similar line profiles are observed for the first few days but this is just a coincidental similarity at this epoch between the Hα profile that has a double minimum and the He I profile that is strongly blended and magnified by the normalization by a factor of at least 5.

The minima of the features from Hα and He I λ5876 are obviously separated from the phase when He I first develops a defined minimum. From day 11 to day 22 the velocities for both lines decline slightly but the separation between them remains essentially constant. From day 22 to day 34 the velocities for both lines is nearly constant.

These velocity measurements provide evidence that H-

lines are formed in a region that is expanding ≈ 4000 km s^{-1} faster than the layer in which He-lines are produced. In the first days after the explosion, opacity in the hydrogen-rich shell conceals all of the material that it surrounds. As the density of the H region is diluted by expansion of the SN, opacity is reduced and when it becomes optically thin, the helium-rich layer below is exposed. In SN 2011dh this happens about day 11.

4.2. *Mass of the Hydrogen Envelope*

Velocity measurements of H I and He I in Type IIb supernovae 2011dh, 2008ax and 1993J provide enough information to compare the relative masses of the high-velocity, hydrogen-rich shells that surrounded the progenitors.

From a basic formula for the optical depth of the hydrogen layer we derive a simple model for the mass of the hydrogen shell. We assume that the first detection of He-features occurs at the the time when the surrounding H-rich layer becomes optically thin. Therefore:

$$\tau_H = 1 = \kappa_T \times \rho \times dR \quad (1)$$

where κ_T is the electron scattering opacity, ρ is the density and dR is the thickness of the H layer. We also assume homologous expansion for the SN, so $R \sim v_H \times t_{He}$. The density is taken to be constant and we make a substitution: $\rho \propto M/R^3$. Then we obtain:

$$M_H \propto (v_H \times t_{He})^2 \quad (2)$$

where v_H is the velocity of the outer edge of the hydrogen shell and t_{He} is the time after the explosion when the He layer is first observed. Thus t_{He} represents the time when the optical depth in H envelope reaches $\tau = 1$.

For all three of the SN IIb, the blue edge of the Hα absorption feature at the time of the first He I measurements is ≈ 20000 km s^{-1}. Accepting v_H as a constant makes the mass of the hydrogen-rich shell directly proportional to the square of the time from explosion to helium detection.

We have shown that for SN 2011dh, $t_{He} \approx 11$ days, and from the literature we find for SN 2008ax, $t_{He} \approx 4$ days (Chornock et al. 2011; Taubenberger et al. 2011) and for SN 1993J, $t_{He} \approx 18$ days (Barbon et al. 1995). The values for t_{He} suggest that the mass of the hydrogen shell surrounding the progenitor of SN 2011dh must be between the masses of the shells for SN 2008ax and 1993J.

Using Equation 2 we calculate:

$$M_H(SN\ 2011dh) \approx 8 \times M_H(SN\ 2008ax)$$

$$M_H(SN\ 2011dh) \approx 0.3 \times M_H(SN\ 1993J)$$

Supporting evidence is provided by the times required for the luminosity to decline from the initial shock heated maximum to the minimum between the thermal and radiation peaks. Again, SN 2011dh is between the other SN IIb. The time to minimum is ≈ 4 days for SN 2011dh, ≈ 1 day for SN 2008ax (Chornock et al. 2011; Taubenberger et al. 2011) and ≈ 9 days for SN 1993J (Richmond et al. 1994, 1996).

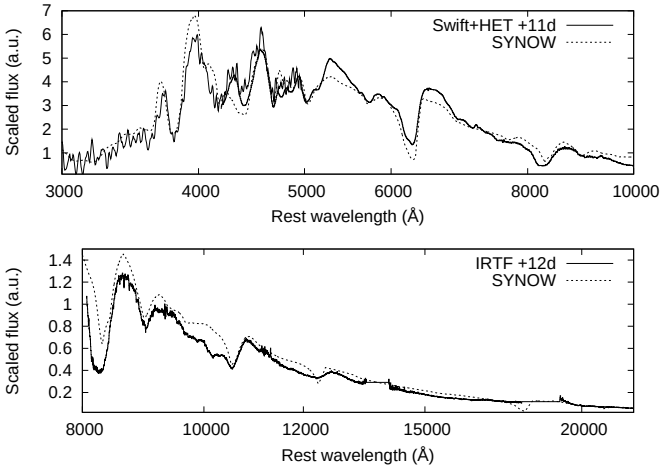

FIG. 9.— SYNOW model spectrum (dashed line) and a combined *Swift*/HET/IRTF spectrum (solid line) from days 11 and 12. The top panel shows the UV-optical region (3000–10000 Å), while the bottom panel shows the NIR (0.8-2.2 μm). with an overlap of ≈ 2000 Å. A detailed discussion of SYNOW modeling is given in § 5.

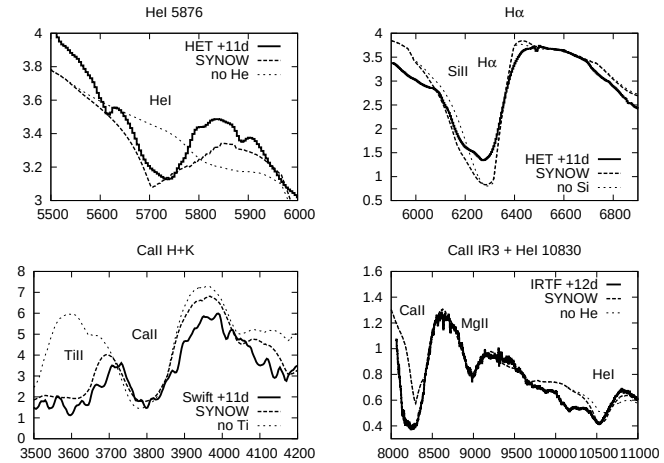

FIG. 10.— SYNOW model (dashed line) and the OIR data from Figure 9 with each panel zoomed in on specific spectral features: He I λ5876 (top left), Hα (top right), Ca II H&K (bottom left), and the Ca II IR3 plus He I λ1.0830 (bottom right). A comparison spectrum from which specific ions have been removed is plotted as the dotted line in each panel: He I is omitted in the top left and lower right panels, Si II is omitted in the upper right, and Ti II and Co II are omitted in the lower left. In each case the fit with the dashed line is better than the fit with the dotted line. A detailed discussion of SYNOW modeling is given in § 5.

5. THE MODEL SPECTRA

Figure 9 shows the combined *Swift*/HET/IRTF spectrum of SN 2011dh (solid line) obtained 11 and 12 days after the explosion plotted with a model spectrum covering 0.3–2.2 μm (dashed line) created with the parametrized modeling code SYNOW (Branch et al. 2003).

The SYNOW model successfully fits the shape of the continuum and accounts for the presence of most spectral features. The optical depth profile is assumed to be a function of velocity: $\tau = \tau(v_{\rm min}) \times (v/v_{\rm min})^{-n}$, where $v_{\rm min}$ is the minimum velocity for a given ion. The following ions (with their reference optical depths) are included in the model: H I (10), He I (0.2), Mg II (0.7), Si II (1),

Ca II (50), Ti II (1), Fe II (1), and Co II (1).

The best SYNOW fit to the complete OIR spectrum is achieved with a power-law index of $n = 6$, a temperature of $T_{BB} = 9000$ K, the velocity of H lines at $v_{\rm phot} = 12000$ km s^{-1} and the velocities of all other lines at $v_{\rm phot} = 9000$ km s^{-1}. These are parameters for a simple line-fitting model and should not be considered physically precise. But the SYNOW results clearly imply that the H line-forming region is located at a higher expansion velocity than the region forming the other lines. This is consistent with the observed separation of H I and He I velocities described in § 4.1.

5.1. *Early Evidence for He I*

SYNOW models can help determine whether or not He I is present in the spectra of SN 2011dh before day 16 when He I absorption features are positively identified. Tentative detections of He I as early as day 11 have been discussed and we seek confirmation from the models for these marginal identifications. To facilitate a detailed comparison of the model to the data, Figure 10 zooms in on individual features found in the full spectrum as displayed in Figure 9.

The top left panel shows that the weak absorption feature near 5750 Å (solid line) is most accurately modeled (dashed line) when He I is included with a low optical depth (0.2). Note that the flux scale makes this feature appear stronger that it is relative to the other features in Figure 10. The model does not reproduce the line-profile but it matches the size and location of the feature. The dotted line shows that a model without He I generates a poor fit to the data. The lower right panel of Figure 10 shows that the feature observed near 10500 Å in the day 12 data (solid line) is primarily due to Paγ (dotted line). But the model fits the data better when He I is included (dashed line).

Thus the SYNOW models suggest that He I may be present 11 days after the explosion even though He I does not produce strong absorption features at this phase. This result is not a detection but it is consistent with the discussion in § 3.2 that presents tentative evidence for features of He I $\lambda\lambda$5876,1.0830 in the day 11 and 12 spectra.

5.2. *Hα Features with Two Components*

We use SYNOW to explore the double bottom found in the Hα profile of early spectra from SN 2011dh. The Hα feature is displayed in the upper right panel of Figure 10. The data (solid line) show that the blue component on day 11 is weaker than found in earlier data but still forms distinct notch in the blue side of the profile. The dashed line is from a model that includes Si II at the same velocity as He I and although it produces a deeper absorption than observed, it shows a notch near 6200 Å that is similar in shape to the observed feature. The dotted line is from a model without Si II and it fails to reproduce the observed inflection.

SYNOW can also produce a notch like the one found in the data when we include a high-velocity hydrogen line-forming region at 15000 km s^{-1} in addition to the H layer that forms the primary absorption at 12000 km s^{-1}. We model the HV region with a shallower optical depth profile (n= 5 instead of 6). The model with HV hydrogen only generates a detectable blue component for Hα. It does not generate similar HV notches for the other H I lines. That result is consistent with the observations that do not find HV components (notches at 15000 km s^{-1}) for other H I lines (Figure 5).

In this case SYNOW provides two plausible answers to the question about the source of the two component line-profile, but it does not give clear guidance to help us chose between them.

5.3. *Ca II Features*

The bottom left panel of Figure 10 shows that the Ca II H&K λ3945 feature (solid line) is successfully fit with a SYNOW model using a $n = 6$ optical depth profile (dashed line). But the same model does not fit the observed Ca II infrared triplet (IR3, λ8579) seen in the bottom right of Figure 10. The IR3 forms a stronger and more extended absorption than the $n = 6$ model used to fit Ca II H&K. The model can be improved with respect to the IR3 feature by using a shallower optical depth profile ($n = 5$) or by inserting a HV Ca II layer, but both of these solutions produce spectra that are incompatible with the observed Ca II H&K profile. The unusual IR3 profile may be caused by line blending and not HV Ca II but we are unable to reproduce the observations of Ca II IR3 with any of the other ions expected to be found in Type II SN atmospheres (Hatano et al. 1999).

5.4. *UV Flux Deficit*

We also use SYNOW models to explore the steep drop in the continuum flux of SN 2011dh at the blue end of the *HST*/STIS spectrum compared to other SN IIb (Figure 4). This wavelength region is included in the lower left panel of Figure 10, but at this phase the data are from *Swift*/U-grism observations. The model spectrum plotted with a dashed line matches the data (solid line) reasonably well and contributions from both Ti II and Co II are required to fit the observed UV-continuum level. The dotted line is produced by a model that omits both Ti II and Co II and it clearly has excess flux at wavelengths less than 3700 Å. Despite the suggestion from SYNOW that Ti II and Co II are present, individual absorption features from Ti II and Co II are not identified in the *Swift* data from days 10 and 11 or the *HST* from day 24.

6. THE LIGHT CURVES

Figure 3 displays light curves for SN 2011dh in 12 filters covering 4–34 days after the explosion. The first photometric observations in our sample were made on June 4.2 UT which is less than 4 days after the estimated time of explosion. For all figures and tables we express the times of observation in whole days relative to the estimated date of explosion. Data were obtained with *Swift* filters: *UVW2*, *UVM2*, *UVW1*, and *U*, FLWO/KeplerCam filters: *u', B, V, r'* and *i'*, and FLWO/PAIRITEL filters: J, H, K_s. Individual measurements are listed in Tables 3, 4, and 5. The data for bands from *UVW1* through *i'* were fit with a second order polynomial to estimate the peak luminosities and the times of maximum brightness (Table 2).

Evidence for cooling from the initial shock-heated peak is revealed by the rapid decline in brightness for the *U*-band and bluer passbands. Maund et al. (2011);

Arcavi et al. (2011); Bersten et al. (2012) also note a steep decline in the brightness of SN 2011dh at longer wavelengths from data obtained prior to our initial observations.

In our sample, minima are reached on day 5 for *u'*, day 6 for *U*-band and day 7 for *UVW1*. The UV light curves subsequently rise toward a second peak as radioactivity in the core begins to provide the luminosity. At the epoch of our first observations the light curve for the *B*-band is at minimum and passbands ($Vr'i'JHK_s$) have passed their minima and are already rising toward the radiation peak.

All references to "peak" or "maximum" in the following discussion refer the observations in our sample. This epoch covers the second, or radiation powered peak.

The *U*-band peak occurs on day 16 and the time to reach maximum brightness in each passband is farther from the date of explosion as the filter wavelength increases. SN 2011dh reached a *B*-band peak of 13.39 mag on day 18.7 ± 0.5 and a *V*-band peak of 12.44 mag on day 20.6 ± 0.5. The exact dates and magnitudes of the JHK_s maxima are uncertain because we lack NIR photometry after day 24 although inspection of Figure 3 suggests that the NIR light curves are within a day or two of their maxima on day 24.

Figure 3 shows that light curves for all bands experience a relatively steep initial rise in brightness with a noticeable change in slope between days 9–12 to a more gradual rate of increase. This phase corresponds to the initial detection of He I. From that phase through the time of maximum brightness the rate of increase is slower. After the peak in each band the decline is almost linear through the end of our data on day 34. This pattern is similar in all bands from *UVW1* to *H* with the phase of the changes occurring earlier at shorter wavelengths.

The light curve for *UVM2*, which is the shortest wavelength filter in our sample, declines steeply from the thermal peak through about day 15 but the subsequent radioactive diffusion is at too low a temperature to revive the light curve. The luminosity in *UVW2* is essentially flat from day 6 through day 23 which is the time of bolometric maximum. *UVW1* is the bluest filter to exhibit a radiation powered second peak.

The transmission curves of the *Swift*/UVOT *UVW1* and *UVW2* filters have extended red tails so the measured flux in these bands includes a contribution from the red side that is beyond the intended wavelength region. We have shown that SN 2011dh has a very low UV flux during the time of our observations, and it is likely that there are significant contributions from optical wavelength regions to the *Swift* measurements in these filters. This "red leak" may contribute to the differences in timing of the minima and overall LC shape between the *UVM2* band and the *UVW1* and *UVW2* bands.

6.1. *Photometric Colors*

B- and *V*-band colors for SN 2011dh are plotted by phase in Figure 11. At day 4, the optical minus NIR colors ($B-J, B-H, V-J, V-H$) are ≈ 0.5 mag redder than optical minus optical colors at this early phase. The optical minus NIR colors rapidly become bluer at about 0.035 mag/day through day 9 while the optical minus optical colors change little through day 11.

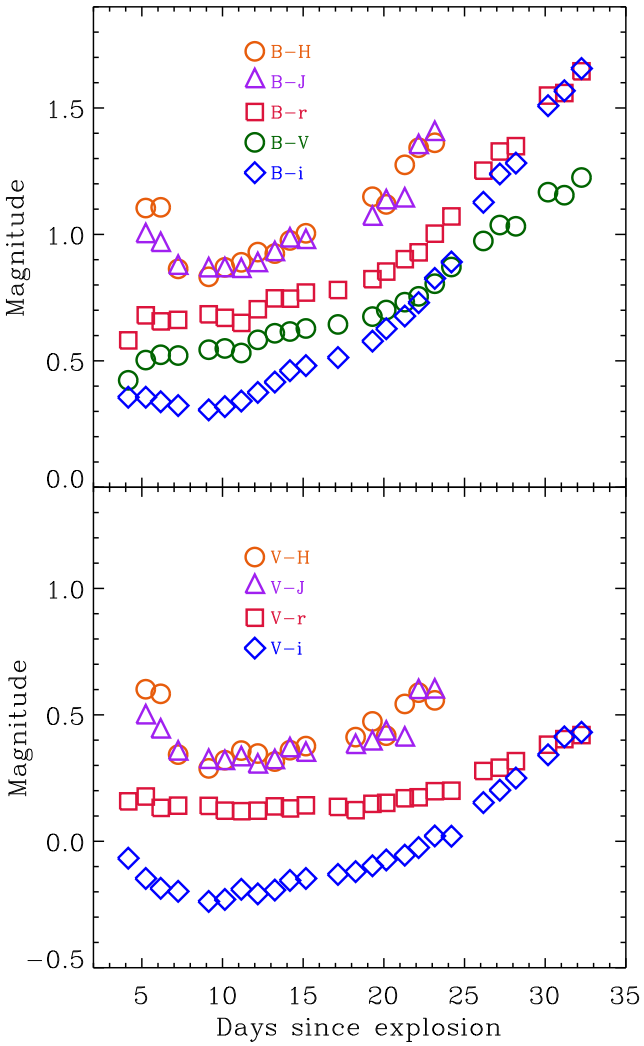

FIG. 11.— B- and V-band colors for SN 2011dh. The optical minus NIR colors are redder at the earliest observations and decline rapidly through day 9 while optical minus optical colors are bluer in the initial observations and remain nearly constant over days 4–9. All colors redden from day 10 through day 34 which indicates the atmosphere is cooling.

Near day 9 the optical minus NIR colors reach a minimum and immediately start reddening but at a much slower rate of change. The timing of these minima coincides with transparency in the H shell since He I is first detected on day 11. This is also the phase when measured velocities of most absorption features stop their rapid decline (Figure 7). From day 10 through the time of maximum brightness ($\approx$ day 21) all colors shift gradually to the red indicating that the atmosphere is cooling. After maximum, the rate of reddening increases as expansion cools the SN. The times of peak for each filter are given in Table 2.

The $B-V$ color evolution in SN 201dh is similar to that of SN 1993J with a period of reddening through about day 8 followed by a very gradual reddening for about two weeks and then a steeper increase (Barbon et al. 1995; Richmond et al. 1996). $B-V$ in SN 2011dh is ≈ 0.2 mag greater from day 4 to day 22 but very close to $B-V$ in SN 1993J from day 22 though the end of our observations.

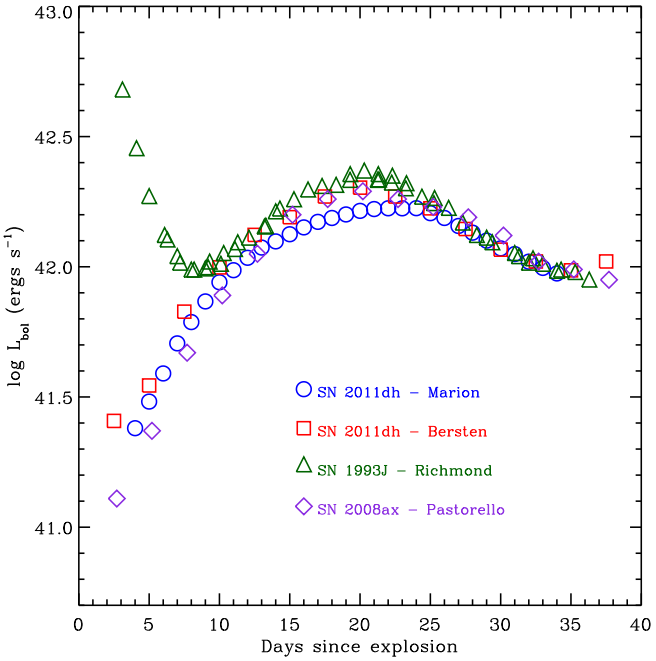

FIG. 12.— Comparing bolometric light curves of three SN IIb. The UVOIR bolometric light curve of SN 2011dh from this paper is displayed with blue circles. The data are given in Table 8. Also plotted are bolometric light curves for SN 2011dh (red squares) from Bersten et al. (2012), SN 2008ax (purple diamonds) (Pastorello et al. 2009) and SN 1993J (green triangles)(Richmond et al. 1994). The maximum luminosity, time of maximum and decline from maximum are similar for all three SN IIb. (§ 7).

From day 4 to day 20, $B-V$ development in SN 2008ax is very similar to the $B-i'$ behavior observed in SN 2011dh. The color gets bluer from the initial measurement, reaches a minimum near 0.2 mag on day 12 and then begins to redden. By day 22, $B-V$ in SN 2008ax is close to the same values found in SN 201dh and SN 1993J. For both SN 1993J and 2008ax $B-V$ stops increasing about day 40.

The $V-R$ color curve of SN 2011dh is generally similar to $V-R$ color behavior in SN Ib and SN Ic found by Drout et al. (2011). These SN types are similar to SN IIb in that they are core-collapse events with little or no hydrogen in the spectra. The mean $V-R$ values from Drout et al. (2011) display an early decline through day 12 (with respect to the explosion), a period of little change through day 20, and an increase through about day 36. The $V-R$ curve in SN 2011dh is slightly flatter but $V-i'$ is a close match.

7. THE BOLOMETRIC LIGHT CURVE

A bolometric light curve for SN 2011dh was constructed from UVOIR data obtained by KeplerCam and PAIRITEL ($u'BVr'i'JHK_s$) and is displayed in Figure 12. The data are given in Table 8. The magnitudes were converted to quasi-monochromatic flux densities using the filter details listed in Table 2. Measurements were corrected for Galactic reddening $E(B-V)=0.035$ mag using the total-to-selective extinction ratios for all filters given in Schlegel et al. (1998).

We sampled the SED at the central wavelength of each observed passband and integrated by wavelength using a simple trapezoidal rule. The missing flux for wavelengths greater than the K-band were approximated by integrating the Rayleigh-Jeans tail of a blackbody starting at the measured K-band flux, between $\lambda_c(K)$ and infinity. The missing UV-region was determined by assuming zero flux at 3000 Å and approximating the SED with a straight line between 3000 Å and $\lambda_c(u')$. This method was verified by integrating an UV SED constructed from the *Swift* UV filters in the same ways as described for the KeplerCam and PAIRITEL filters.

The maximum bolometric luminosity of 1.7×10^{42} erg s^{-1} was reached 23 days after the explosion. Total measurement uncertainties are $\approx 10.5\%$ of the bolometric flux which is $\pm1.8\times10^{41}$ erg s^{-1} at peak. NIR contributions account for $\approx 35\%$ of the total bolometric flux from day 4 through maximum and then increase to 52% by day 34 (Table 8). Wavelengths below 3000 Å that are not covered by our ground-based photometry provide only a negligible contribution to the total bolometric flux.

Figure 12 displays the bolometric light curve for SN 2011dh with blue circles. A second bolometric LC for SN 2011dh constructed from a different data set by (Bersten et al. 2012) is plotted with red squares. Bolometric light curves for two other Type IIb are included: SN 1993J (green triangles) (Richmond et al. 1994) and 2008ax (purple diamonds) (Pastorello et al. 2008).

Bersten et al. (2012) use $D=7.1$ Mpc for the distance to M 51 in their calculations and we rescale their data using our distance estimate of $D=8.05$ Mpc. Richmond et al. (1994) construct a UVOIR bolometric LC for SN 1993J from observed *UBVRI* data by estimating the temperature at each phase with optical data and then adding the blackbody flux that would be emitted outside the *UBVRI* window. A UVOIR light curve for SN 2008ax was obtained by Pastorello et al. (2008) by compiling several data sets to construct a new UVOIR LC for SN 1993J and then rescaling the *UBVRI* data for SN 2008ax data with the same fractional NIR contribution estimated for SN 1993J at each phase.

Kumar et al. (2013) report that the bolometric LC for SN IIb 2011fu reached $\approx 4.8\times10^{42}$ erg s^{-1} at 27 days after the explosion. SN 2011fu also had a slower decline from the thermal peak than SN 1993J and did not reach the minimum between peaks until about 14 days after the explosion. The $B-V$ colors after maximum are similar in shape and offset by about 0.2 mag when compared to colors found in the other three SN IIb.

Figure 12 shows that the maximum bolometric luminosities and the overall light curve shapes are similar for SN IIb 2011dh, 2008ax and 1993J from day 10 to day 34. The match is particularly good after maximum. $B-V$ colors after maximum are also very similar for all three SN. This result shows that the mass of the hydrogen shell surrounding the progenitors only affects the early, cooling phase of light curves from Type IIb supernovae. The similarities in the magnitudes of the bolometric peaks suggest that the ^{56}Ni yield must have been close to the same for each explosion. Thus the progenitors of these three SN IIb appear to have been similar in composition and mass beneath hydrogen envelopes that had significant differences.

One of the evolutionary models (single star or binary system) may be responsible for the progenitors of SN 2011dh, 2008ax and 1993J and Type IIb supernovae

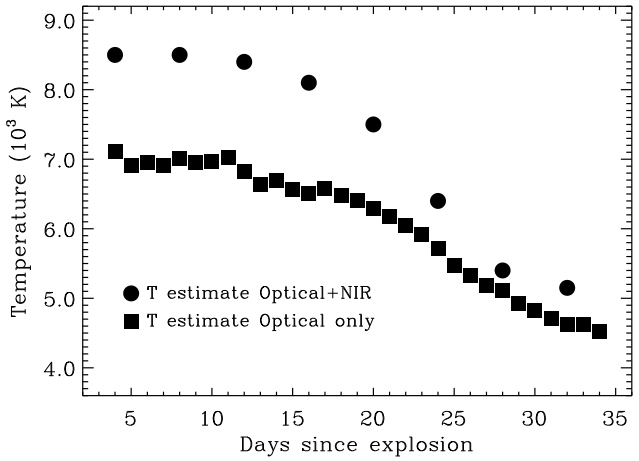

FIG. 13.— Estimated temperature by phase for SN 2011dh from 4–34 days after the explosion. The circles are temperature estimates based on blackbody fits that include NIR data. The squares are temperature estimates made using optical data only.

from this channel may be standard candles. The other evolutionary track could produce SN IIb like 2011fu.

7.1. *Temperatures*

Figure 13 shows estimated temperatures for SN 2011dh by phase. The filled circles are temperature estimates obtained by fitting blackbody (BB) curves by eye to a full set of OIR SEDs from passbands *BVr'i'JHK*. The filled squares are temperature estimates using only optical SEDs (*BVr'i'*) that are fit to BB curves by minimizing χ^2. Both methods suggest very little change in temperature from day 4 to day 12 that is consistent with nearly constant values for $B-V$ during this epoch. The phase at which the temperature begins to decline is also when the H-layer becomes transparent and reveals the He-region below.

Figure 2 shows BB curves fit to the OIR spectra obtained 8, 12, and 16 days after the explosion. We find a very consistent relationship between BB temperature curves, the complete OIR spectra, and the SEDs for OIR passbands *u'BVr'i'JHK*. We do not plot SEDs on the already crowded Figure 2, but the temperature curves fit to OIR spectra pass directly through the SEDs for passbands *Vi'JHK* at all three phases. The circles in Figure 13 represent the temperature of a BB curve that we chose by eye to fit the *Vi'JHK* SEDs. Line blending is less severe in the NIR than at UV and optical wavelengths which puts an additional premium on the PAIRITEL data that are available through day 24. After day 24, we replace the *JHK* SEDs by integrating the Rayleigh-Jeans tail of a blackbody.

The SEDs for *u'*, *B* and *r'* are less reliable. For example, the *r'*-band SED is complicated by the large Hα absorption feature in spectra of SN 2011dh. BB curves that pass through the *V*-band and *i'*-band SEDs, are always a little below the *r'*-band SED. The suppressed continuum flux for SN 2011dh at less than 4000 Å means that a blackbody is not a realistic representation of data from SN 2011dh at these wavelengths. That means that any method of estimating temperature with BB curves does not actually fit data to the peak of the BB curves.

Temperature estimates made by fitting to a wider wavelength range that includes the NIR appear to be more effective than estimates made with optical data alone. Our estimate for the day 4 temperature is 8500 K which is $\approx$ 1000 K higher than the temperature estimate for a day 3 optical spectrum provided by Arcavi et al. (2011) and $\approx$ 700 K higher than the estimate of Bersten et al. (2012).

8. SUMMARY AND CONCLUSIONS

Our results show details of chemical layering in SN 2011dh that have not been previously reported for SN IIb. We demonstrate the importance of NIR measurements for line identification, temperature estimates and bolometric estimates.

We present the earliest secure identification of He I lines in spectra of SN 2011dh. The presence of He I determines the classification of Type IIb supernovae. We show that He I is a likely contributor to the spectra as early as 11 days after the explosion but blending prevents definitive identification before NIR spectra reveal distinct features of He I $\lambda\lambda$1.0830,2.0581 sixteen days after the explosion.

A UV spectrum from *HST*/STIS shows a significant deficit in continuum flux at wavelengths below 4000 Å when compared with other SN IIb. SYNOW model spectra are used to demonstrate that Ti II and Co II are responsible for the suppressed UV flux. We also use SYNOW models to investigate blended features and to confirm the presence of He I in a spectrum obtained on day 11 in spite of the fact that He I absorption features are not clearly identified.

Velocities of H I, He I, Ca II, and Fe II features are measured from 4 days after the explosion through day 34. Strong H I features are evident in the earliest spectra of SN 2011dh but the first evidence for He I does not appear until day 11. Ca II and Fe II velocities continue to decline after H I and He I velocities become constant at about day 17. The relative velocities and velocity decline rates found in SN 2011dh are similar to observations of SN IIb 1993J and 2008ax.

We show that early measurements of both H I and He I are important for understanding the transition from the early phases when hydrogen dominates the spectra to later times when H fades and He becomes dominant. Using measurements of four H I lines and five He I lines, we show that the H line-forming region and the layer producing He lines are separated by $\approx$ 4000 km s^{-1} at all phases. We suggest that this gap is consistent with a H-rich shell that is optically thick after the explosion and conceals material beneath it. Opacity in the H shell is reduced by expansion until the slower-moving He-rich region is uncovered about day 11.

We present photometry of SN 2011dh from 12 filters and construct a bolometric light curve with maximum luminosity of $1.7 \pm 0.2 \times 10^{42}$ erg s^{-1} on day 23. The NIR fraction of the total bolometric luminosity in SN 2011dh is found to be greater than 35% at day 4 and more than 50% one month after the explosion. The bolometric maxima and the light curve shapes after maximum are similar for SN 2011dh and two other SN IIb 2008ax and 1993J. The $B-V$ colors after maximum are also a close match. This suggests that the progenitors had similar masses and composition when they exploded.

Using the time intervals from the explosion to the first evidence for He I in SN 2011dh and SN IIb 1993J and

2008ax, we show that the mass of the hydrogen shell surrounding the progenitor of SN 2011dh was about eight times greater the hydrogen shell around the SN 2008ax but three times less than the mass of the shell that enclosed SN 1993J. Thus different masses for the hydrogen shell only affect the early light curves of Type IIb supernovae and by the time of maximum brightness they may be standard candles.

The progenitor of SN 2011dh has recently been identified as a yellow supergiant star. Successful models based on that progenitor will have to match the detailed velocity measurements and light curve data presented here.

Acknowledgments:
The CfA Supernova Program is supported by NSF grant AST-1211196 to the Harvard College Observatory. RPK was supported in part by the National Science Foundation under Grant NSF PHY-1125915 to the Kavli Institute for Theoretical Physics. J.V. is supported by Hungarian OTKA Grants K-76816 and NN-107637, NSF grant AST-0707769, and Texas Advanced Research Project ARP-009. JCW is supported by NSF grant AST-1109801. ASF acknowledges support from a NSF Graduate Research Fellowship and a NASA Graduate Research Program Fellowship. Support for program number 12540 was provided by NASA through a grant from the Space Telescope Science Institute, which is operated by the Association of Universities for Research in Astronomy, Inc., under NASA contract NAS5-26555. KT has also received support from Hungarian OTKA Grant K-76816.

GHM thanks John Rayner, Alan Tokunaga, Bill Golish, David Griep, Paul Sears, and Eric Volquardsen at the IRTF for supporting target-of-opportunity observations. GHM is a visiting Astronomer at the Infrared Telescope Facility, which is operated by the University of Hawaii under Cooperative Agreement no. NNX-08AE38A with the National Aeronautics and Space Administration, Science Mission Directorate, Planetary Astronomy Program. We thank Gaspar Bakos, David Latham, and Matthew Holman for making FLWO observing time available. We acknowledge the work of C. Klein on the PAIRITEL mosaic data reduction pipeline and we reference observations made with the Vatican Advanced Technology Telescope. The authors make frequent use of David Bishop's excellent webpage listing recent supernovae and valuable references associated with them: www.rochesterastronomy.org/snimages/.

REFERENCES

Arcavi, I. et al. 2011, ApJ, 742, 18
Arnett, W. D., Bahcall, J. N., Kirshner, R. P. and Woosley, S. E. 1989, ARA&A, 27, 629
Barbon, R., et al. 1995, A&AS, 110, 513
Benvenuto, O. G., Bersten, M. C. and Nomoto, K. 2013 ApJ, 762, 74
Bersten, M. C. et al. 2012, ApJ, 757, 31
Bietenholz, M. F. et al. 2012 ApJ, 751, 125
Branch, D., Baron, E. A., and Jeffery, D. J. 2003, Supernovae and Gamma-Ray Bursters, 598, 47
Chevalier, R. A. and Soderberg, A. M. 2010, ApJ, 711, 40
Chiosi, C. and Maeder, A. 1986, ARA&A, 24, 329
Chornock, R. et al. 2011, ApJ, 739, 41
Chugai, N. N., Chevalier, R. A. and Utrobin, V. P. 2007 ApJ, 662, 1136
Cohen, M., Wheaton, W. A., and Megeath, S. T. 2003, AJ, 126, 1090
Cushing, M. C., Vacca, W. D. and Rayner, J. T. 2004, PASP 116, 362
Drout, M. et al. 2011, ApJ, 741, 97
Fabricant et al., PASP 1998, 110, 79
Feldmeier, J. J., Ciardullo, R., and Jacoby, G. H. 1997, ApJ, 479, 231
Friedman, A. S. 2012, Ph.D. Thesis
Filippenko, A. V., Matheson, T., and Ho, L. C. 1993, ApJ, 415, 103
Hatano, K., Branch, D., Fisher, A., Millard, J., and Baron, E. 1999, ApJs, 121, 233
Hicken, M. et al. 2007, ApJ, 669, L17
Hicken, M. et al. 2012, ApJS, 200, 12
Hill, G. J. et al. 1998, Proc. SPIE, 3355, 375
Horesh, A. et al. 2012, ApJ submitted (arXiv1209.1102)
Jeffery, D. J. et al. 1994 ApJL, 421, 27
Kochanek, C. S. 2009, ApJ, 707, 1578
Krauss, M. I. et al 2012, ApJL, 750, 40
Kumar, B. 2013, MNRAS, tmp, 821
Lewis, J. R. et al. 1994, MNRAS., 266, 27
Marion, G. H. et al. 2011, The Astronomers Telegram, 3435
Matheson, T. et al. 2005, AJ, 129, 2352
Maund, J. R. et al. 2011, ApJL, 739, 37
Mazzali, P. A. et al. 2005 ApJ, 623, 37
Murphy, J. W. et al. 2011, ApJ, 742, 4
Nomoto, K. et al. 1993, Nature, 364, 507
Nomoto, K. I., Iwamoto, K., and Suzuki, T. 1995, PhR, 256, 173
Pastorello, A. et al. 2008, MNRAS, 389, 131
Pastorello, A. et al. 2009, MNRAS, 394, 2266
Podsiadlowski, P., Hsu, J. J. L., Joss, P. C., and Ross, R. R. 1993, Nature, 364, 509
Prieto, J. L. and Hornoch, K. 2011, The Astronomers Telegram, 3433
Ramsey, L. W. et al. 1998, Proc. SPIE, 3352, 34
Rayner. J. T. et al. 2003, PASP, 115, 362
Reiland, T., Griga, T., Riou, A., and Lamotte Bailey, S. Central Bureau for Astronomical Telegrams, CBET No. 2736
Richmond, M. W. et al. 1994, AJ, 107, 1022
Richmond, M. W. et al. 1996, AJ, 112, 732
Ritchey, A. M. and Wallerstein, G. 2012, ApJ, 748, 11
Roming, P.W., 2009, ApJ, 704, 118
Rush, B., Malkan, M. A., and Edelson, R. A. 1996, ApJ, 473, 130
Schlegel, D. J., Finkbeiner, D. P., and Davis, M. 1998, ApJ, 500, 525
Schmidt, B. et al. 1993, Nature, 364, 600
Silverman, J. M. et al. 2011, The Astronomers Telegram, 3398
Soderberg, A. et al. 2012, ApJ, 752, 78
Szczygiel, D. M., Gerke, J. R., Kochanek, C. S., and Stanek, K. Z. 2012, ApJ, 747, 23
Taubenberger, S. et al. 2011, MNRAS., 413, 2140
Tonry, J. L. et al. 2001, ApJ, 546, 681
Tsvetkov, D. Yu. et al. 2012, Peremennye Zvezdy, vol.32, no. 6 (arXiv:1207.2241)
Tully, R. B. 1988, Nearby Galaxies Catalogue, NBGC.C, 0000
Van Dyk, S. D. et al. 2011, ApJ, 741, 28
Van Dyk, S. D., Filippenko, A. V., Fox, O., Kelly , P. and Smith, N. 2013, The Astronomers Telegram, 4850
Vinkó, J. et al. 2012, A&A, 540, 93
Wheeler, J. C. et al. 1993, ApJ, 417, 71
Woosley, S. E., Eastman, R. G., Weaver, T. A., Pinto, P. A. 1994, ApJ, 429, 300

TABLE 1
Spectrocopic Observations

Date (UT)[a]	Instrument	Range (Å)	R	Exp. (s)
Jun 4.2	FAST	3480 - 7420	1350	900
Jun 5.2	FAST	3480 - 7420	1350	1500
Jun 6.1	HET	4200 - 10100	280	900
Jun 6.2	FAST	3480 - 7420	1350	1200
Jun 7.2	FAST	3480 - 7420	1350	1200
Jun 8.2	FAST	3480 - 7420	1350	900
Jun 8.4	IRTF	8000 - 24000	1200	1800
Jun 9.2	FAST	3480 - 7420	1350	900
Jun 9.9	SWIFT	2000 - 4600	150	900
Jun 11.1	SWIFT	2000 - 4600	150	1135
Jun 11.2	HET	4200 - 10100	280	900
Jun 12.4	IRTF	8000 - 24000	1200	1800
Jun 14.2	HET	4200 - 10000	280	900
Jun 16.4	IRTF	8000 - 24000	1200	1800
Jun 17.2	HET	4200 - 10100	280	900
Jun 22.2	HET	4200 - 10100	280	900
Jun 24.0	HST	2160 - 10230	4300	3600
Jun 25.2	FAST	3480 - 7420	1350	720
Jun 26.2	FAST	3480 - 7420	1350	720
Jun 27.2	FAST	3480 - 7420	1350	720
Jun 28.3	FAST	3480 - 7420	1350	840
Jun 29.2	HET	4200 - 10100	280	900
Jun 30.3	FAST	3480 - 7420	1350	900
Jul 1.2	FAST	3480 - 7420	1350	900
Jul 2.2	FAST	3480 - 7420	1350	960
Jul 4.2	FAST	3480 - 7420	1350	900

Note. — The time of explosion is May 31.5 UT and the time of B-max is June 18.7 UT.
[a] All observations in 2011.

TABLE 2
Peak Magnitudes and Filter Details

Band	M_{peak} (mag)	D_{peak}[a]	N_{obs}	λ_{mid}(Å)
		PAIRITEL[b]		
K_s	< 11.91[c]	> 24[c]	18	21590
H	< 11.91[c]	> 24[c]	18	16620
J	< 12.02[c]	> 24[c]	17	12350
		KeplerCam		
i'	12.45	23.2	27	7747
r'	12.26	21.7	27	6217
V	12.44	20.6	26	5375
B	13.17	18.7	25	4270
u'	14.42	16.6	14	3525
		Swift		
V	12.63	20.9	37	5468
B	13.39	19.0	39	4392
U	13.90	16.5	40	3465
UVW1	15.53	15.1	27	2600
UVM2	...	...	27	2246
UVW2	...	...	27	1928

[a] Whole days with respect to the time of explosion.
[b] Filter details from Cohen, Wheaton, & Megeath (2003).
[c] Final measurements on day 24 precede the peak by a day or two.

TABLE 3
Photometric Measurements with the FLWO 1.2m and KepCam

Date (UT)[a]	u'	u' err	B	B err	V	V err	r'	r' err	i'	i' err
55716.2	15.676	0.012	15.115	0.011	14.692	0.010	14.534	0.015	14.759	0.020
55717.2	15.754	0.023	14.866	0.009	14.363	0.008	14.186	0.010	14.510	0.013
55718.2	15.563	0.016	14.580	0.009	14.056	0.009	13.924	0.012	14.242	0.017
55719.2	15.307	0.011	14.264	0.007	13.743	0.008	13.602	0.011	13.941	0.014
55721.1	14.971	0.154	13.849	0.006	13.305	0.010	13.165	0.016	13.543	0.020
55722.1	14.854	0.134	13.677	0.007	13.128	0.010	13.007	0.013	13.358	0.017
55723.2	...	...	13.549	0.011	13.018	0.011	12.899	0.013	13.208	0.013
55724.2	...	...	13.462	0.006	12.879	0.009	12.758	0.012	13.087	0.019
55725.2	...	...	13.397	0.006	12.788	0.009	12.650	0.012	12.981	0.015
55726.2	...	...	13.351	0.004	12.735	0.006	12.605	0.008	12.890	0.010
55727.2	...	...	13.295	0.006	12.667	0.008	12.525	0.013	12.814	0.017
55729.2	...	...	13.199	0.007	12.555	0.009	12.419	0.011	12.686	0.016
55730.2	...	...	...	...	12.514	0.008	12.391	0.010	12.634	0.012
55731.3	...	...	13.165	0.006	12.490	0.008	12.342	0.010	12.587	0.014
55732.1	14.456	0.008	13.164	0.009	12.463	0.008	12.311	0.011	12.537	0.015
55733.3	...	...	13.183	0.008	12.451	0.010	12.281	0.013	12.506	0.014
55734.2	14.578	0.006	13.211	0.004	12.456	0.005	12.282	0.006	12.481	0.007
55735.2	...	...	13.293	0.004	12.488	0.003	12.290	0.005	12.467	0.005
55736.2	14.877	0.010	13.386	0.008	12.515	0.010	12.315	0.011	12.495	0.014
55738.2	15.261	0.011	13.650	0.006	12.676	0.005	12.398	0.005	12.523	0.006
55739.2	15.510	0.011	13.810	0.005	12.773	0.004	12.482	0.007	12.571	0.007
55740.2	...	...	13.900	0.006	12.868	0.003	12.551	0.003	12.618	0.003
55742.2	16.059	0.018	14.236	0.009	13.069	0.010	12.687	0.011	12.727	0.016
55743.2	16.215	0.024	14.324	0.008	13.169	0.004	12.765	0.003	12.756	0.003
55744.2	16.443	0.026	14.474	0.008	13.249	0.006	12.829	0.008	12.818	0.010

[a] Average time of observation for a sequence with multiple filters. Estimated date of explosion: MJD=55712.5

TABLE 4
Photometric Measurements with PAIRITEL

Date (UT)[a]	J	J err	H	H err	K_s	K_s err
55717.1	13.875	0.193	13.762	0.535	13.607	0.369
55718.2	13.624	0.153	13.473	0.401	13.497	0.341
55719.2	13.398	0.123	13.400	0.370	13.077	0.255
55720.2	13.196	0.100	13.154	0.292	13.027	0.296
55721.2	12.993	0.082	13.017	0.255	12.969	0.185
55722.2	12.821	0.068	12.807	0.205	12.702	0.151
55723.2	12.696	0.061	12.659	0.178	12.510	0.153
55724.2	12.585	0.055	12.532	0.155	12.317	0.122
55725.1	12.477	0.050	12.473	0.151	12.427	0.125
55726.2	12.377	0.054	12.375	0.148	...	...
55727.2	12.327	0.050	12.291	0.130	12.214	0.162
55728.2	12.230	0.044	12.140	0.119	12.047	0.156
55730.2	12.143	0.041	12.102	0.110	11.933	0.133
55731.2	12.105	0.038	12.016	0.097	12.000	0.101
55732.2	12.039	0.036	12.045	0.105	11.934	0.108
55733.2	12.051	0.036	11.908	0.088	11.986	0.030
55734.2	11.868	0.081	11.868	0.077	11.976	0.039
55735.2	11.898	0.099	11.931	0.217	11.931	0.217

[a] Average time of observation for a sequence with multiple filters. Estimated date of explosion: MJD=55712.5

TABLE 5
Photometric Measurements with *Swift*

Date (UT)[a]	UVW2	*UVM2*	UVW1	U
55716.0	16.315	15.941	15.405	14.956
55716.7	16.610	16.195	15.567	15.096
55717.7	16.837	16.510	15.815	15.140
55719.0	16.743	16.700	15.862	14.880
55720.6	17.000	16.840	15.760	14.477
55721.8	16.807	17.196	15.689	14.285
55723.1	16.939	17.236	15.597	14.142
55723.8	16.784	17.384	15.679	14.076
55725.1	16.890	17.166	15.637	13.990
55726.6	16.980	17.605	15.595	14.015
55728.8	16.970	17.660	15.600	13.930
55729.2	16.860	17.420	15.610	13.870
55730.3	16.800	17.410	15.560	13.890
55731.5	16.890	17.620	15.530	13.910
55732.5	16.890	17.660	15.630	13.930
55733.5	17.010	17.670	15.640	13.990
55734.4	17.030	17.590	15.700	14.080
55735.7	16.970	17.810	15.820	14.250
55736.2	17.170	17.960	15.840	14.310
55737.2	17.450	17.800	16.030	14.560
55738.8	17.390	17.790	16.246	14.820
55740.2	17.699	18.772	16.512	15.134
55741.4	17.778	18.292	16.674	15.348
55741.8	17.894	18.437	16.668	15.494
55742.7	...	...	...	15.463
55743.8	18.474	19.155	17.104	15.900
55745.2	18.117	18.955	17.027	16.020
55746.1	18.540	18.322	17.319	16.185

[a] Average time of observation for a sequence with multiple filters. Estimated date of explosion: MJD=55712.5

TABLE 6
Velocity Measurements of H and He Lines (km s^{-1})

Epoch[a]	Hα	Hβ	Hγ	Paβ	He I 5876	He I 6678	He I 7065	He I 1.0830	He I 2.0581
4	15400	13800	14100	...	...	...	...	...	...
5	14500	13000	13900	...	...	...	...	...	...
6	14100	12700	13600	...	...	...	...	...	...
7	13700	12200	13500	...	...	...	...	...	...
8	13500	12000	13400	...	...	...	...	...	...
9	13300	11600	13100	...	...	...	...	...	...
10	...	...	12600	...	...	...	...	...	...
11	13100	11000	12500	...	8400	...	...	...	...
12	...	...	...	12200	...	...	...	8200	...
13	...	...	...	...	...	...	...	...	...
14	12500	10800	...	...	7600	...	...	...	...
15	...	...	...	12000	...	...	...	...	...
16	...	...	...	...	...	...	...	8000	7200
17	12400	10700	...	...	7500	...	...	...	...
18	...	...	...	11900	...	...	...	...	...
19	...	...	...	...	...	...	...	...	...
20	...	...	...	...	...	...	...	...	...
21	...	...	...	...	...	...	...	...	...
22	12100	10600	...	...	7500	6500	...	...	...
23	...	...	...	...	...	...	...	...	...
24	12100	10900	...	...	7600	6600	7400	...	...
25	11900	11000	...	...	7400	6600	7200	...	...
26	12100	11000	...	...	7600	6900	7200	...	...
27	12000	10800	...	...	7600	7100	7100	...	...
28	11900	10800	...	...	7500	7200	7100	...	...
29	12000	10700	...	...	7400	7600	7000	...	...
30	12000	10900	...	...	7500	7300	6900	...	...
31	12000	10900	...	...	7600	7300	7000	...	...
32	11900	10800	...	...	7700	7200	7000	...	...
33	...	...	...	...	...	...	...	...	...
34	11800	10800	...	...	7800	7100	6800	...	...

[a] Whole days with respect to the time of explosion.

TABLE 7
Velocity Measurements of Ca II and Fe II Lines (km s^{-1})

Epoch[a]	Ca II 3945	Ca II 8579	Fe II 4561	Fe II 5018	Fe II 5169	Fe II 1500
4	13700	···	12700	···	11400	···
5	12500	···	12300	12200	11000	···
6	12600	14300	11800	11500	10900	···
7	12500	···	11700	11200	10700	···
8	12400	···	11900	10900	10100	9500
9	12100	···	11400	10700	10000	···
10	11800	···	···	···	···	···
11	11800	13000	10500	8800	8800	···
12	···	···	···	···	···	9100
13	···	···	···	···	···	···
14	···	12700	8900	8000	7800	···
15	···	···	···	···	···	···
16	···	···	···	···	···	8700
17	···	12100	8800	7600	7500	···
18	···	···	···	···	···	···
19	···	···	···	···	···	···
20	···	···	···	···	···	···
21	···	···	···	···	···	···
22	···	10800	8200	6900	6900	···
23	···	···	···	···	···	···
24	10600	10000	7500	6800	6900	···
25	10800	···	7300	6600	6600	···
26	10700	···	6900	6500	6400	···
27	10700	···	···	···	6400	···
28	10300	···	···	···	6100	···
29	···	9600	···	···	···	···
30	9900	···	···	···	6000	···
31	9800	···	···	···	5800	···
32	9500	···	···	···	5700	···
33	···	···	···	···	···	···
34	9200	···	···	···	5300	···

[a] Whole days with respect to the time of explosion.

TABLE 8
Bolometric Luminosity ($u'BVr'i'JHK_s$)

Epoch[a] (Days)	Total Flux [b] (10^{42} erg s^{-1})	NIR Flux (10^{42} erg s^{-1})	NIR Fraction
4	0.24	0.09	0.37
5	0.30	0.11	0.36
6	0.39	0.14	0.36
7	0.51	0.17	0.34
8	0.61	0.21	0.34
9	0.74	0.24	0.33
10	0.87	0.30	0.34
11	0.97	0.33	0.34
12	1.08	0.37	0.34
13	1.19	0.41	0.35
14	1.25	0.44	0.35
15	1.33	0.47	0.35
16	1.42	0.51	0.36
17	1.49	0.54	0.36
18	1.54	0.56	0.36
19	1.59	0.58	0.36
20	1.64	0.61	0.37
21	1.67	0.62	0.37
22	1.68	0.64	0.38
23	1.68	0.68	0.40
24	1.68	0.72	0.43
25	1.61	0.71	0.44
26	1.54	0.70	0.45
27	1.43	0.67	0.47
28	1.35	0.64	0.47
29	1.26	0.61	0.48
30	1.18	0.58	0.49
31	1.12	0.57	0.50
32	1.05	0.53	0.51
33	0.99	0.51	0.52
34	0.94	0.49	0.52

[a] Whole days with respect to the time of explosion.
[b] Total measurement uncertainties are $\approx 10.5\%$ of the bolometric flux.